DESIGN AND CONSTRUCTION OF PORTABLE LOCALIZED SURFACE PLASMON RESONANCE DEVICE FOR DETECTION OF BIOLOGICAL MOLECULES

A Thesis Submitted to
the Graduate School of Engineering and Sciences of
İzmir Institute of Technology
in Partial Fulfillment of the Requirements for the Degree of

MASTER OF SCIENCE

in Biotechnology

by
Aytaç GÜL

July 2017
İZMİR

We approve the thesis of **Aytaç GÜL**

Examining Committee Members:

Prof. Dr. Volga BULMUŞ
Department of Bioengineering, İzmir Institute of Technology

Assist. Prof. Dr. Ümit Hakan YILDIZ
Department of Chemistry, İzmir Institute of Technology

Prof. Dr. Gülperi ÖKTEM
Department of Histology and Embryology, Medical School, Ege University

27 July 2017

Prof. Dr. Volga BULMUŞ
Supervisor, Department of Bioengineering
İzmir Institute of Technology

Assoc. Prof. Dr. Engin ÖZÇİVİCİ
Head of the Department of Biotechnology
and Bioengineering

Prof. Dr. Aysun SOFUOĞLU
Dean of the Graduate School of
Engineering and Sciences

ACKNOWLEDGEMENTS

I would like to thank my former supervisor, Dr. Hadi M. Zareie for supporting me to study in a topic that I preferred. I would not have been succeed in the thesis without his support. I am very grateful to him for acting me like a father and for the invaluable advice he has given me.

I would like to thank my late supervisor, Prof. Dr. Volga BULMUŞ, for her generous support. The answers to my many questions and editorial advice for this thesis have been priceless. Also, I would like to express my deepest thanks to her for helping me in the difficult times I have experienced and giving me numerous suggestions about life. I would also like to thank Aysel TOMAK for her assistance with experiments and for years of friendship and her valuable help with in all matters.

To my parents, father, mother, and my sister and my brother, for their bottomless love, support. I could not have done this without them.

ABSTRACT

DESIGN AND CONSTRUCTION OF PORTABLE LOCALIZED SURFACE PLASMON RESONANCE DEVICE FOR DETECTION OF BIOLOGICAL MOLECULES

Point-of-care devices giving rapid results in non-laboratory settings have become important for biosensor applications in a wide range of fields including medical, food, agriculture and pharmaceutical. This work aims to produce a portable device based on localized surface plasmon resonance spectroscopy (LSPR-S) as a potential biosensor platform that can be used in non-laboratory settings for rapid detection of biological molecules at high sensivity.

The thesis can be divided into two parts: In the first part, the design and construction of the device including both the mechanical and electronic parts are presented. The mechanical section includes the integration of the parts to build the device and microchannels designed with the aid of a three-dimensional drawing program Solid Works 2015®. The second step of the construction process was the installation of electronic components onto the device. The electronic part consists of a light source, fiber optic cables, a spectrometer and a temperature sensor. In conclusion, a portable LSPR-S device with an integrated microchannel system has been produced, which potentially allows analysing low volumes of sample without the need to label the molecules.

The second part of the thesis covers the studies towards the preparation and application of sensing platforms for the LSPR-S device constructed to enable the rapid detection of biological molecules at high sensitivity. These included the preparation of gold nanorods and nanoparticles-based LSPR detection of model antibody-antigen and bacteria- bacteriophage interactions, respectively. Studies conducted in this section have led to the conclusion that the LSPR-based biosensor platforms developed in this thesis are promising solutions to overcome current challenges in biosensor applications.

ÖZET

BİYOLOJİK MOLEKÜLLERİN TESPİTİ İÇİN TAŞINABİLİR LOKALİZE YÜZEY PLAZMON REZONANS CİHAZININ TASARIMI VE İMALATI

Laboratuar ortamı dışında hızlı sonuçlar veren hasta başı cihazlar sağlık, gıda, tarım ve ilaç gibi geniş bir yelpazede biyosensör uygulamaları için önemli olmuştur. Bu çalışma, yüksek hassasiyette biyolojik moleküllerin hızlı tespiti için laboratuar dışı ortamlarda kullanılabilecek potansiyel bir biyosensör platformu olarak lokalize yüzey plazmon rezonans spektroskopisine (LSPR-S) dayanan taşınabilir bir cihaz üretmeyi amaçlamaktadır.

Bu tez 2 kısma ayrılmıştır: Tezin ilk kısmında, cihazın mekanik ve elektronik kısmındaki parçaların tasarımı ve üretimi gösterilmektedir. Mekanik bölüm cihazın parçalarının üç boyutlu çizim programı Solid Works 2015 yardımıyla çizildikten sonra üretilmesi ve mikro-kanalların mekanik kısma entegrasyonunu içerir. Üretim prosesinin ikinci kısmı elektronik aksamların cihaz üzerine montajıdır. Elektronik kısım; ışık kaynağı, fiber optik kablolar, spektrometre ve sıcaklık sensöründen oluşmaktadır. Sonuçta, potansiyel olarak molekülleri işaretlemeye ihtiyaç duymadan düşük hacimlerde örneklerin analizine imkan sağlayan mikrokanal sistemi entegre edilmiş portatif bir LSPR-S cihazı üretilmiştir.

Tezin ikinci kısmı, biyolojik moleküllerin yüksek hassasiyetle hızlı bir şekilde tespit edilmesini sağlayan LSPR-S cihazı için sensör platformlarının hazırlanması ve uygulanmasına yönelik çalışmaları kapsıyor. Bunlar, altın nanorodların ve altın nanoparçacıkların hazırlanmasını ve sırasıyla antikor-antijen ve bakteri ve bakteriofaj ilişkilerinin LSPR temelli tespitini içermektedir. Bu bölümde yapılan çalışmalar, bu tezde geliştirilen LSPR esaslı biyosensör platformlarının, biyosensör uygulamalarındaki mevcut zorlukların üstesinden gelmeye umut verici bir çözüm olduğuna karar verilmiştir.

TABLE OF CONTENTS

LIST OF FIGURES

Figure **Page**

LIST OF TABLES

CHAPTER 1

INTRODUCTION

This thesis focuses on the construction of a portable localized surface plasmon resonance (LSPR) spectroscopy device for rapid detection of intermolecular interactions between biological molecules in non-laboratory settings. Also, it accordingly covers the production of gold nanorod and gold nanoparticle-based nanobiosensors for detection of biological molecules such as a sialic acid residue overexpressed in certain cancers and bacteria, respectively. The second chapter of the thesis gives background information about biosensors and LSPR spectroscopy including working principles of biosensors, types of biosensors, theory of LSPR, and literature review of LSPR spectroscopy. Chapter 3 describes the experimental methods used in construction of the LSPR device and preparation of nanobiosensors. Chapter 4 gives the results obtained throughout the study and their discussions. Chapter 5 summarizes the conclusions derived and future recommendations.

CHAPTER 2

BACKGROUND

2.1.What is a Biosensor?

Biosensors are analytical devices that convert a biological response into an electrical signal also, allows rapid and cheap analysis of characteristic properties of materials. Their applications include detection of organisms, and biological molecules, disease monitoring, and drug discovery and also detection of presence of environment pollutants[1]. Biosensor technology is growing fast combining biological, chemical, and physical sciences together with engineering for broad range of applications[2]. The first term of biosensor was introduced in 1956 by L. C. Clark, Jr who is also inventor of Clark electrode[3]. Enzyme electrode was later suggested by Clark and Lyons in 1962[4]. This was followed by the development of functional enzyme electrodes for glucose detection[5]. Guilbault and Montolva[6] were then discovered potentiometric enzyme biosensor to detect urea. Finally, first commercial biosensor based on Clark's glucose analyser idea was produced in 1975 by Yellow Springs Instrument Company (YSI)[7]. In the late 1970s, several other authors pave the way for arising new concept of biosensors. Table 1 displays the historical review of biosensors in between 1970–1992 years.

Table 2.1. Important events in the development of biosensors throughout history[1]

1970 Discovery of ion-sensitive field-effect transistor (ISFET) by Bergveld[8].
1975 Fibre-optic biosensor for carbon dioxide and oxygen detection by Lubbers and Opitz[9].
1975 First commercial biosensor for glucose detection by YSI[7].
1975 First microbe-based immunosensor by Suzuki et al[10].
1982 Fibre-optic biosensor for glucose detection by Schultz[11].
1983 Surface plasmon resonance (SPR) immunosensor by Liedberg et al[12].
1984 First mediated amperometric biosensor: ferrocene used with glucose oxidase for glucose detection[13].
1990 SPR-based biosensor by Pharmacia Biacore[9].
1992 Handheld blood biosensor by i-STAT[9].

2.2.The Working Principle of Biosensor

In general, biosensor consists of two main components; a bioreceptor and a transducer. Bioreceptor is a biomolecule such as enzymes, antibodies, cell, nucleic acid that is used to recognize the analyte which is the target molecule for receptor. Transducer is a second equipment of biosensor that is used to convert biorecognition events into measureble signal[14].

The biosensor working mechanism is displayed in Figure 2.1. Firstly, analyte diffuses from bulk solution to the bioreceptor immobilized sensor and react selectively with bioreceptor. This event causes a change in properties such as optical, electronic etc depending on transducer used. The modification in biosensor surface is converted into a signal that is processed and displayed by a transducer such as optical, calorimetric, and electrochemical[15].

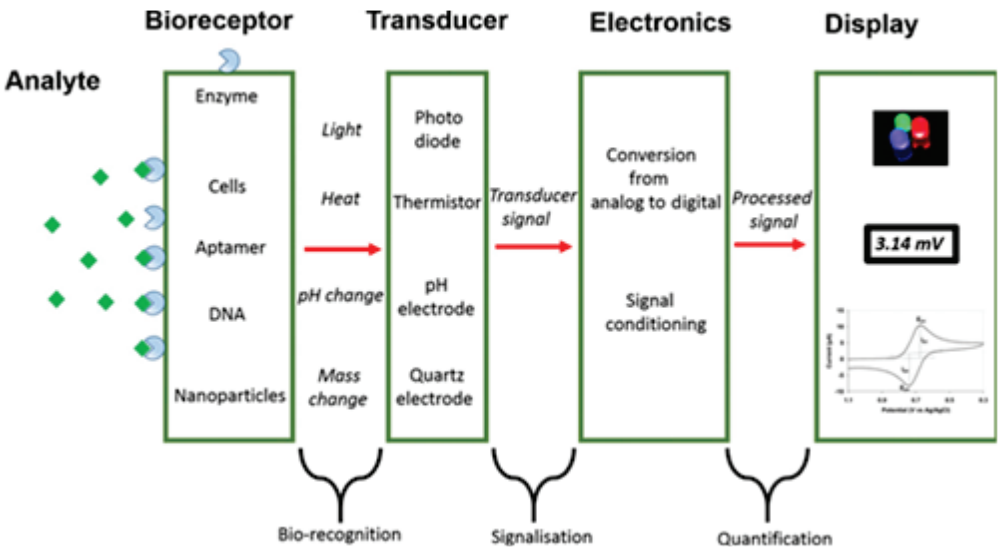

Figure 2.1. Schematic representation of working principle of biosensor1

2.3.Characteristics of a Biosensor

Basic characteristics of biosensor includes mainly four parameters. These are[16];

- **Linearity:** It is the variety of analyte concentration. Linearity of the sensor should be high for the detection of high and low substrate concentrations.
- **Sensitivity:** It is known as one of the important properties of biosensors. Sensivity is the response of the sensor to analyte concentration‘s unite change.
- **Selectivity:** Presumably, it is the most significant charecterictic of biosensors. Selectivity is the ability of sensor to detect target analyte.
- **Stability:** It is defined as a change in its baseline over a required long time incubation period.

In addition to above parameters, there are also some other significant features required when a biosensor is designed. These are response time, reproducibility, detection limit and life time. In addition to these factors, a biosensor ought to be cheap, easy to use, biocompatible and durable under hard conditions[17].

2.4.Applications of Biosensors

Biosensors have various applications including detection of industrial toxins and chemicals, military and defence industry[18], drug discovery and more. One of the major application fields of biosensors is in diagnosis of diseases[19]. For example, electrochemical biosensors can be used for detection of protein based cancer markers[20]. Also biosensors can be used as a tools for monitoring presence of bacteria in foods to ensure food quality, safety[21], nutritive values [21] and food presentableness [22]. There are also numerous studies on environment monitoring[23] to determine pollution level in air[24], land[25], water[26]. In addition, biosensors are helpful to measure various ions in fermentation products, microorganisms products such as hormones, vaccines, single cell proteins[27-28]. Examples of application areas of biosensors are schematically shown in Figure 2.2[1].

Figure 2.2. Basic application fields of biosensors[1]

2.5.Types of Biosensors

Biosensors are categorized according to the working principle of their transducers. Most known transducers are classified into three groups: electrochemical, optical and piezoelectric[29]. Each classes of transducers has sub-classes. Also, with technological progress, new types of transducers have been developed.

2.5.1.Electrochemical Biosensors

Electrochemical biosensors are the most widely used class of biosensors. They are the first commercialized biosensors, introduced first by Clark and Lyons[30]. The working principle of electrochemical biosensors are based on the conversion of the chemical information, which is produced by the biorecognition event of biomolecules immobilized on the sensor surface and target analyte into measurable electrical signal[31-32]. Most common types of electrochemical biosensors are potentiometric, amperometric and voltammetric biosensors[31, 33].

2.5.2.Piezoelectric Biosensors

Acoustic wave biosensors or piezoelectric biosensors use the piezoelectric effect and transform pressure orforce to an electrical signal. Working principle of this kind of biosensor is based on the detection of the change in the mass density on piezolectric crystal[34]. They are cheap devices and do not require expensive electronic equipments for processing data. Their small size and flexibility offer real-time detection of diseases [35].

2.5.3.Optical Biosensors

When compared with other types of biosensors, optical biosensors present more options for detection methods such as absorbance, fluorescence, luminescence, reflectance, light scattering, or refractive index[36]. They also provide vast opportunities which conventional methods do not offer, such as high sensivitiy, selectivity, real time and label-free detection of many materials[37]. Optical biosensors have been used in health care, biomedical research area, analysis of wide variety of biological materials and homeland security[38]. Schematic illustration of optical biosensors is displayed in Figure 2.3[37]. Most widely known optical biosensors are surface plasmon resonance biosensor (SPR) and localized surface plasmon resonance biosensor (LSPR).

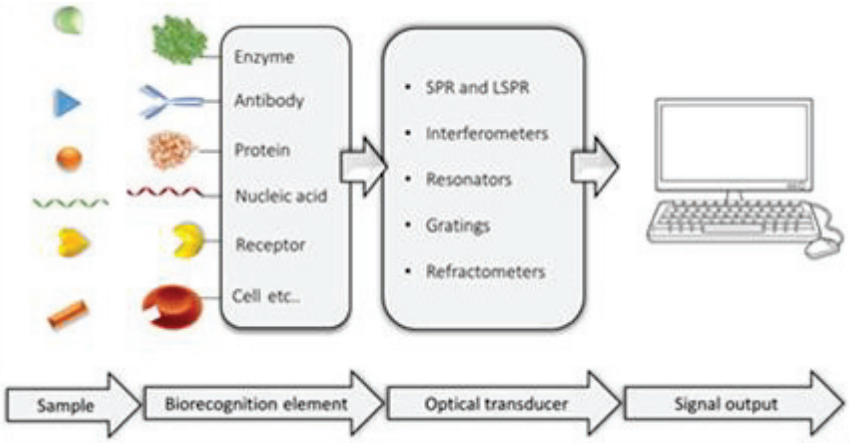

Figure 2.3. Operation Principle of Optical Biosensors[37]

2.6.Localized Surface Plasmon Resonance (LSPR)

This thesis focuses on one of the types of optical sensors that is namely Localized Surface Plasmon Resonance (LSPR). The theory behind the localized surface plasmon resonance is that the sum of absorption and scattering of light in nanoparticles induces the loss of intensity of light that is called extinction. The electric field of incident light with metallic nanoparticles constitutes oscillation from collective electron cloud[39]. This oscillation is called plasmons, in other words, plasmon is a collective oscillation of free electron in accordance with positive ions on metal surface[40].

When plasmons oscillate around nanoparticle surface with a frequency, it is then called localized surface plasmon (LSP) (Figure 2.4A). On the other hand, plasmons are confined on metal or oscillation of plasmons in the form of propagating along the metal surface is called surface plasmon polariton (SPP) (Figure 2.4B)[41].

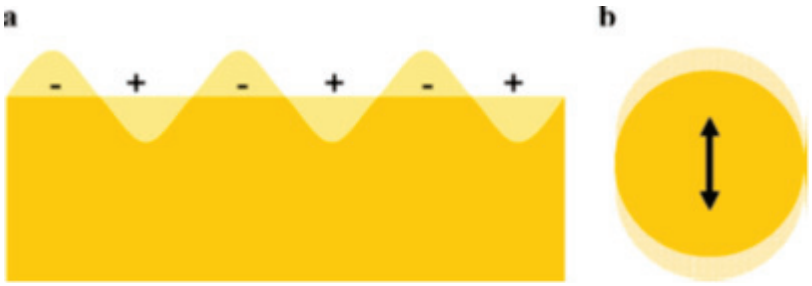

Figure 2.4. Surface Plasmon Polariton (a) Localized Surface Plasmon(b)[41]

2.7.Localized Surface Plasmon Resonance Spectroscopy

Localized surface plasmon resonance spectroscopy is considered to be one of the new generation powerful techniques in nanotechnology and sensing platforms. LSPR spectroscopy presents as an alternative method for various fields[42]. For example, to detect HE4 that causes ovarian cancer, anti-HE4 antibody was used as probe on LSPR surface and the detection limit of HE4 was found to be 4 pM, which indicates well that LSPR can be used to detect low concentrations of analytes[43].

LSPR has advantage of providing high sensitivity of refractive index changes, label-free detection, real-time measurements, reproducibility using nanostructure substrates, and low cost[44]. These advantages make Localized surface plasmon resonance spectroscopy amenable to various fields, such as medical, food safety, environmental monitoring and drug screening[45].

Sensing principle of LSPR spectroscopy is based on wavelength-shift that is caused by the environmental dielectric change resulting from molecular binding events[46]. Also, LSPR peak position is correlated with composition, dimension, and shape of nanomaterials and inter-particle distance of the metallic nanostructures[47]. By changing, the parameters that mentioned above, sensitivity and selectivity of LSPR can be modulated or the size of LSPR spectrometer can be minimized.

There are two widely used running modes of localized surface plasmon resonance spectroscopy. These modes, transmission and reflection, are illustured in Figure 2.5[42].

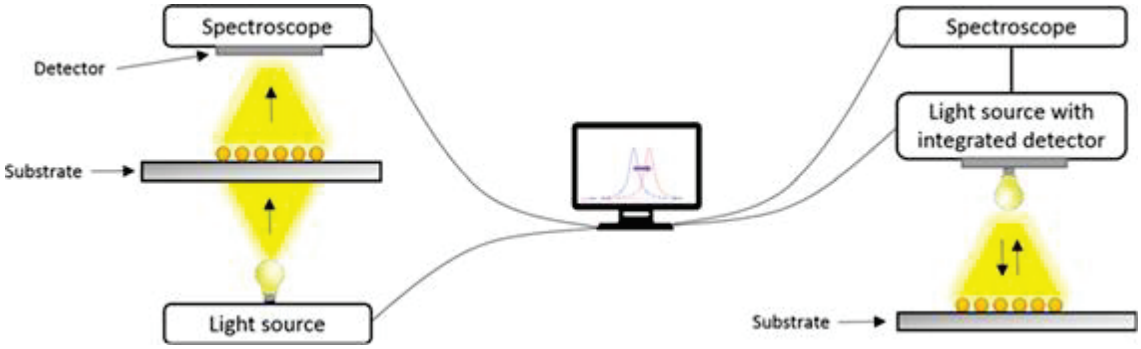

Figure 2.5. Illustration of working modes of LSPR system, transmmision (left), and reflection (right)[42]

2.8.Theory of Localized Surface Plasmon Resonance (LSPR)

Metallic nanoparticles such as gold and silver display a strong optical extinction in visible and near-infrared fields and produce LSPR event that is sensitive to surrounding medium[48]. The intense and strong signals in all surface-enhanced spectroscopies are due to LSPR excitation with selective absorption wavelength[49]. The Mie developed a convenient approach for approximation of the extinction of a metallic nanoparticle in the long wavelength[50].

$$\sigma_{ext} = 9\frac{\omega}{c}\varepsilon_3^{\frac{3}{2}}V_0\frac{\varepsilon_2(\omega)}{[\varepsilon_1(\omega)+2\varepsilon_m]^2+\varepsilon_2(\omega)^2} \quad (2.1)$$

$V_0 = (4\pi/3)R^3$, ω is the angular frequency of the extinction radiation, ε_m is the dielectric constant of the medium surrounding the metal nanoparticles, ε_1 and ε_2 are real and imaginary parts of the dielectric function of the metal nanoparticles, respectively[51]. It is clearly known that LSPR spectrum is highly dependent on metallic nanoparticles shapes. For example, gold nanorods display high sensitivity over other particles shapes. Due to this reason, further equation for non-spherical metallic nanoparticles was shown in Equation 2.2[52-53].

$$\sigma_{abs} = \frac{\omega}{3c}\varepsilon_m{}^{3/2} V \sum_j \frac{\left(1/P_j{}^2\right)\varepsilon_2}{\left[\varepsilon_1 + \{(1-P_j)/P_j\}\right]^2 + \varepsilon_2{}^2} \tag{2.2}$$

j is the three dimensions of the particle , P_j is a depolarization factors and has three sub-class succesively P_A, P_B, and P_C[54]. The depolarization factor changes ε_1 and ε_2, and resulting LSPR peak frequencies are displayed in Equation 2.2.

$$P_A = \frac{1-e^2}{e^2}\left[\frac{1}{2e}\ln\left(\frac{1+e}{1-e}\right) - 1\right] \tag{2.3}$$

$$P_B = P_C = \frac{1-P_A}{2}$$

e is aspect ratio R of the particle [17, 55-56].

$$e = \left[1 - \left(\frac{B}{A}\right)^2\right]^{1/2} = \left(1 - \frac{1}{R^2}\right)^{1/2} \tag{2.4}$$

Equation 2.2 caused arising of two peaks. The first peak is related to transverse plasmon peak from *x*- and *y*-axes, and the second peak belongs to longitudinal plasmon peak from *z*-axis contribution.

In addition, it enables us to find out how to change aspect ratio on LSPR peak position. ε_m is the dielectric constant of metallic nanosphere. Because of this reason, red shift of LSPR peak occurs and also it contribute to increment of sensitivity to the dielectric constant of the surrounding medium[40]. In Equation 2.6 the relationship between LSPR peak and dielectric function of the surrounding medium is displayed[57].

$$\varepsilon_1 = 1 - \frac{\omega_p{}^2}{\omega^2 + \gamma^2} \tag{2.5}$$

ω_p is a plasmon frequency, γ is the damping factor of the bulk metal. When γ is smaller than ω_p, Equation 2.6 is transformed into Equation 2.7 that is more simple form, represented as[40],

$$\varepsilon_1 = 1 - \frac{{\omega_p}^2}{\omega^2} \tag{2.6}$$

When resonance conditions ($\varepsilon_1 = -2\varepsilon_{1m}$), are applied on equation 2.6, equation 2.7 is obtained[40].

$$\varepsilon_{max} = \frac{\omega_p}{\sqrt{2\varepsilon_m + 1}} \tag{2.7}$$

ω_{max} is a frequency of the LSPR peak, wavelength frequency is $\lambda = 2\pi c/\omega$, and dielectric constant of refractive index $\varepsilon_m = n^2$ are inserted in Equation 2.7, Equation 2.8 is obtained[40].

$$\lambda_{max} = \lambda_p\sqrt{2{n_m}^2 + 1} \tag{2.8}$$

λ_{max} is wavelength of LSPR peak and λ_p is the wavelength that is related to frequency of the bulk metal. Finally, direct proportion between the wavelength of the LSPR peak and refractive index was obtained roughly. Also relationship between them allow reducing the detection limit of LSPR or increasing the sensivity[58].

The λ_{max} shifts of LSPR are dependent on the metallic nanoparticle size and the sensitivity of the biomolecules conjugated to particles. Mathematically λmax shifts of LSPR can be described in Equation 2.9, showing the relationship between sensitivity, size morphology and composition of metallic nanoparticles[59].

$$\lambda_{max} = m\Delta n \tag{2.9}$$

Where n is the refractive index. The shift is also proportional to the adsorbate molecule mass[60-61]. Recently, various methods have been developed to probe or detect large shift from metallic nanoparticles and its conjugation with biomolecules[62]. Another way to increase the λ_{max} shift is to use plasmonic labels using AuNPs[63].

2.9.Literature Review of Localized Surface Plasmon Resonance

Nowadays, LSPR spectroscopy-based sensor applications are considered to be the new-generation label-free methods[64]. Additionally, LSPR experimental setups have demonstrated substantial simplification compared to those used in conventional measurement techniques[65]. For these reasons, researchers begin to deepen their research in order to design and develop LSPR based optical biosensors with the help of plasmonic nanomaterials[66].

A large number of papers have been published on the application of the LSPR spectroscopy in biotechnology, nanotechnology and other related fields. These publications are generally on the detection of bacteria-macrophage[67], anti-biotin[68], concanavalin[44], alzheimer disease biomarkers[69], antigen-antibody[70] and streptavidin-biotin[71] and other bio-recognition events[72]. Other applications of LSPR are on chemical detection of molecules in liquid phase such as organo-phosphorous pesticides[73], hydrogen peroxide[74] and ammonia[75].

Van Duyne and co-workers were one of the first groups to investigate biological sensors based on metal nanoparticles using LSPR spectroscopy[76]. Van Duyne and Amanda J. Haes created a nanostructure using natural lithography to develop a sensitive LSPR-based method for detection of Alzheimer disease[69].

Also, Van Duyne and co-workers investigated biotin- streptavidin interaction in great detail using triangular silver nanoparticles fabricated by nanosphere lithography. The biotin- streptavidin system has high binding affinity, it therefore presents a very convenient platform to demonstrate LSPR-based nanoscale affinity biosensors[71].

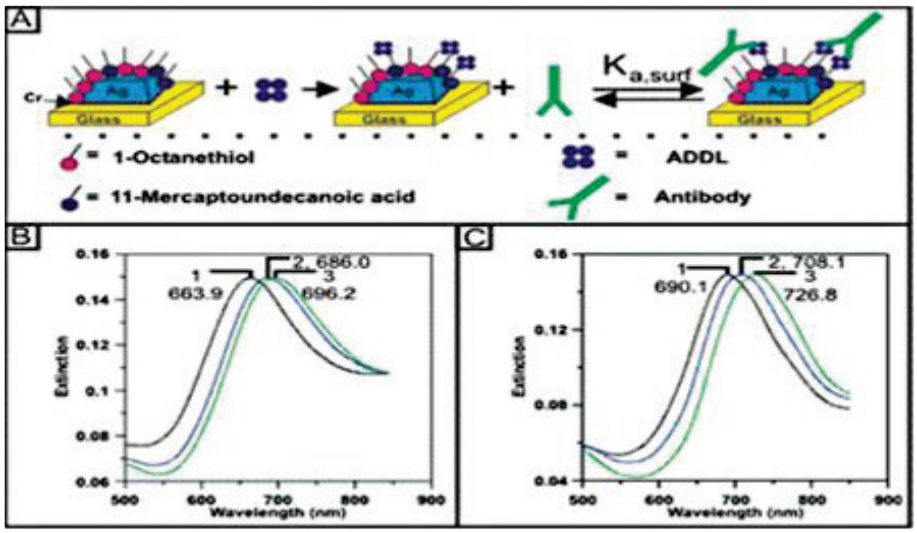

Figure 2.6. (A) Production steps of Ag nanoparticle-based sensor to detect Anti-ADDL. (B) Ag nanobiosensor conjugate at a low concentration of anti-ADDL antibody. Ag nanoparticles functionalized with 1 mM 3:1 1-OT/11-MUA λ_{max} = 663.9 nm, (B-1). After adding 100 nM ADDL λ_{max} = 686.0 nm (B-2) and (B-3) 50 nM anti-ADDL λ_{max} = 696.2 nm. (C) Ag nanobiosensor conjugate at a high concentration of anti-ADDL. Ag nanoparticles functionalized with 1 mM 3:1 1-OT/11-MUA, λ_{max}= 690.1 nm (C-1), (C-2) 100 nM ADDL λ_{max} = 708.1 nm, and (C-3) 400 nM anti-ADDL λ_{max}= 726.8 nm[69]

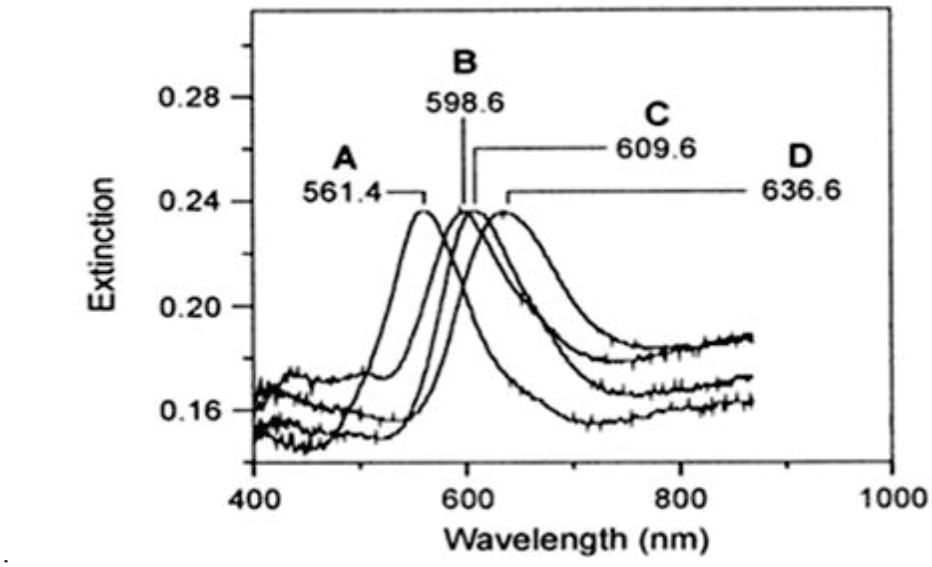

Figure 2.7. Ag nanoparticles modified with biotin for detecting the specific binding of streptavidin. (A) Bare Ag nanoparticles λ_{max}= 561,4 nm. (B) Ag nanoparticles modified with 1 mM 1:3 11-MUA/1-OT λ_{max} =598.6 nm. (C) After Ag nanoparticles conjugate 1 mM biotinλ_{max}= 609,6 nm. (D) Ag nanoparticles with 100 nM SA λ_{max}= 636,6 nm[71]

Xu and co-workers designed and fabricated an immunosensor to detect alfa-fetoprotein using LSPR of gold nanorods. GNRs were produced with seed-mediated method and conjugated with 11-mercaptoundecanoic acid to attach antibodies. Their results showed that the limit of detection of the sensor was 0.25 nM and dynamic range was between 0.25 nM and 14.3 nM. These results indicate that the LSPR spectroscopy works efficiently even at low concentration of samples[77].

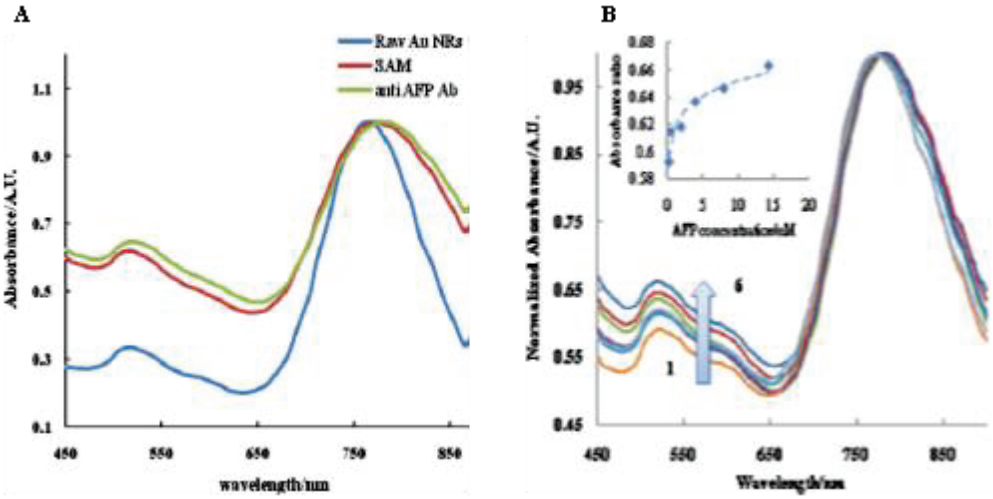

Figure 2.8. (A) LSPR spectra of modified and unmodified gold nanorods. Blue line is bare gold nanorods, LSPR spectrum of red line is 11-mercaptoundecanoic acid modified gold nanorod, green line is anti AFB antibody bound gold nanorod. (B) LSPR spectra of varying concentrations of anti AFP antibody[77]

Lee and colleagues fabricated Au-dots (10-20 nm) on ITO glass substrate using electrochemical deposition method to detect HIV-1. To detect HIV-1, first of all, Au-dots substrate was modified with gp 120 antibody. The substrate was then used to measure various concentrations of HIV-1 particles for determination of limit of detection. Limit of detection of HIV-1 was estimated to be 200 fg/mL that was 10-fold higher than previous reports[78].

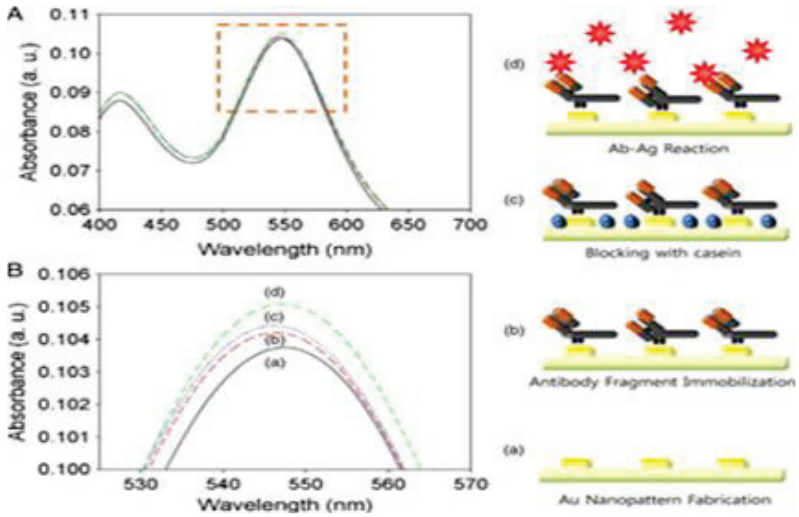

Figure 2.9. (A) LSPR spectrum each conjugation step. (a) Raw Au dots. (b) Au dots were modified antibody. (c) Conjugate with casein. (d) HIV-1 VLPs reacted with substrate. (B) Detailed LSPR spectrum of wavelength between 520 to 570 nm[78]

Bhagawati and colleagues studied real-time imaging of protein and protein interactions with localized surface plasmon resonance spectroscopy using micropatterned AuNPs produced through electrostatic forces. To capture protein, AuNPs were first conjugated with poly ethlyene glycol , then conjugated with poly-L-lysine grafted PEG[79].

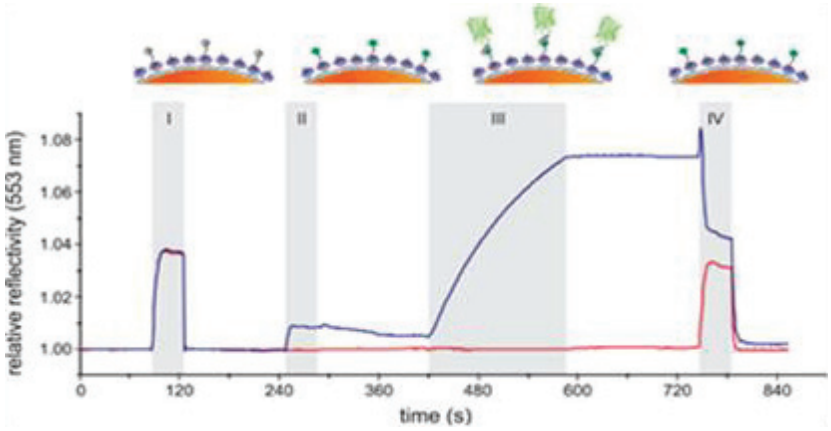

Figure 2.10. LSPR spectrum for each binding step. First, micropatterned AuNPs surface was treated with 250 mM EDTA (I), NTA moieties were injected with Ni(II) ions (II) Injection of 500 nM H6-EGFP (III) Elution with 500 mM imidazole (IV) (blue curve). As a control, protein binding in the absence of Ni(II) ions (red curve)[79]

In brief, LSPR sensing covers a wide range of systems, from simple chips capable of detecting a target analyte, to sophisticated instrumental schemes allowing observation of analyte binding to single nanostructures. A representative selection of LSPR-based biosensor systems is summarized in Table 2.1[80].

Table 2.2. Selected literature examples of LSPR Spectroscopy[80]

Configuration of LSPR sensor	Preparation of recognition interface	Experimental details	Sensitivity
Au NPs (40 nm) in Solution[59].	Au NPs covered with monoclonal anti hFABP. Detection of binding of hFABP	Incubation of Au NP bioconjugate with analyte	Ca. 20 ngml hFABP. Determination of affinity constants in the range 109–1011 mol−1
Au NPs immobilized on silanized glass, NPs enlarged by electroless deposition[81].	Au NPs functionalized with HSA or anti-HSA. Detection of binding of anti-HSA or HSA, respectively	Difference in extinction after binding of analyte in stagnant solution	Minimum detected concentration 100 μgml−1 of HSA
Au NPs (13–50 nm) immobilized on silanized glass[82].	Au NPs functionalized with MPA followed by chemical coupling of biotin. Detection of streptavidin and anti-biotin monoclonal antibody	Kinetics of extinction change during analyte binding in a stirred solution	Detection limit of streptavidin ca. 20nM for 13-nm NPs and 1 nM for 39-nm NPs
Au NPs (40 nm) immobilized on silanized glass[83].	Au NPs functionalized with BSA or HAS	Measurements of transmission spectra in solution	Detection limit ca. 30 nM for anti-HSA
Au NPs (40 nm) immobilized on silanized glass [84-86].	Au NPs functionalized with disulfide polymer carrying receptor. Binding of ConA, HIV1 protease, glycoprotein	Kinetics of extinction change during analyte binding and release	Detection limit of ConA, 1.9 nM; HIV-1, protease, 50 nM; glycoprotein (OVA), 10 0nM

Table 2.3. Selected literature examples of LSPR Spectroscopy (continued)[80]

Au NP (9 nm) film immobilized on fiber after removal of normal claddin[87].	Au NPs functionalized with cystamine followed by coupling of biotin or immobilization of anti-SEB	Laser intensity attenuation, measured using lock-in technique	Detection limit (S/N ratio of 3) 1 nM for streptavidin and 1.4 pM for anti-SEB
Au NPs immobilized on unclad silanized silica fiber[88].	Binding of streptavidin to immobilized biotin	Binding of analytes in a flow cell	Detection limit (S/N ratio of 3) of streptavidin 0.1 nM;
Au NPs immobilized on the end face of a fiber[89].	Binding of streptavidin to immobilized biotin	Binding of analyte in stagnant solution	Optical response measured at 20 μgml-1
Au NPs (40 nm) immobilized on glass[90].	SZ-BSA immobilized on AuNPs followed by exposure to anti-SZ	Light scattering from epiluminescent AuNPs immersed in stagnant solution	Detection limit 20nM for Sz

2.10.Antibody-Antigen Interactions

Antibodies are molecules that are involved in specific immune recognition and secreted from B-cell[91]. The antibody molecule has two remarkable functions: one of the function is to bind specifically molecules from pathogens that create the immune response; the other property is to help other cells and molecules to recover destroying from the pathogen[92]. Antibody molecules are Y-shaped molecules consisting of three same-sized regions and connected each other with flexible bonds[93]. The two arms of the Y end in regions, called V (variable) regions, vary between different antibody molecules[94]. These are involved in antigen binding, whereas the stem of the Y called the C (constant) region is in charge of interacting with effector cells and molecules[95]. The structure of antibody molecules is shown in Figure 2.11[96].

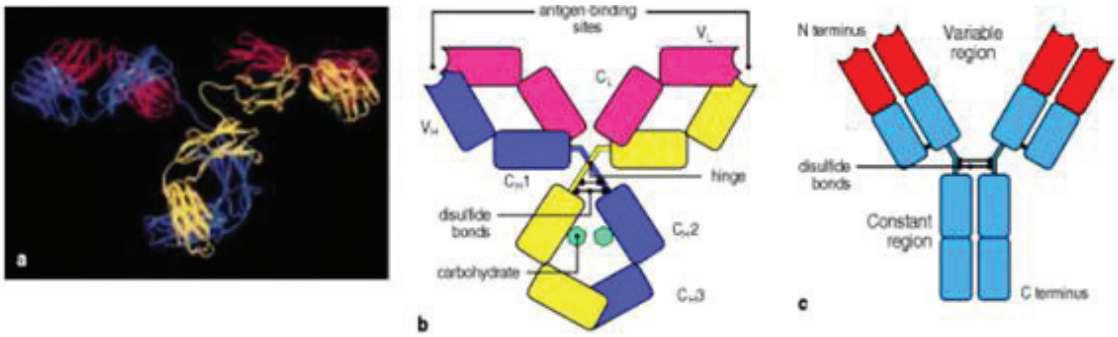

Figure 2.11. Structure of an antibody molecule. (A) Ribbon diagram based on the X-ray crystallographic structure of an IgG antibody. (B) Four-chain composition and the separate domains comprising each chain. (C) Simplified schematic representation of an antibody molecule[96]

The antibodies comprise small proteins of the immunoglobulin family (Ig) consisting of anti-parallel B sheets[97]. Ig consists of the two same light chain of molecular weight of 25 kDa and two heavy chains of 50 kDa, which form the Y shape of antibody molecules[96, 98]. These heavy and light chains are divided into two compartments. First one is that the N-terminus that forms the antigen binding site and the c-portion that determines isotype[99]. Also, the light chain and heavy chain are composed of respectively two Ig and four Ig domains family depending on the antibody isotype[100-101].

The light chains and the heavy chains are attached each other with noncovalent and disulfide bonds interactions[102]. The heavy chain of V region and light chain are linked to form two antigen binding sites to allow the antibody to bind strongly to the antigen[103]. When the V_H and V_L domains are linked to the antibody, hypervariable loops in these domains come together to form the complementarity-determining regions (CDR1, CDR2, and CDR3), in other words the antigen binding site[104]. This CDR region consists of a combination of heavy and light chains and identifies the specificity of the antigen. Also three CDR regions come together to form the surface of the antibody[105].

The interaction between an antibody and its antigen can be disrupted by high salt concentrations[106], extremes of pH[107], detergents, and sometimes high concentrations of the pure epitope[108]. The binding is therefore a reversible noncovalent interaction. The forces, or bonds, involved in these noncovalent interactions are illustrated in Figure 2.12[109].

Noncovalent forces	Origin	
Electrostatic forces	Attraction between opposite charges	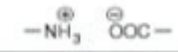
Hydrogen bonds	Hydrogen shared between electronegative atoms (N,O)	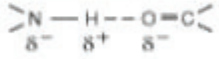
Van der Waals forces	Fluctuations in electron clouds around molecules oppositely polarize neighboring atoms	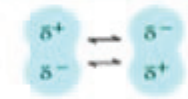
Hydrophobic forces	Hydrophobic groups interact unfavorably with water and tend to pack together to exclude water molecules. The attraction also involves van der Waals forces	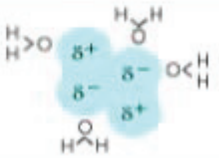

Figure 2.12. Non-covalent forces that hold together the Antigen-Antibody complex[109]

2.11.Bacteria-Phage Interaction

Bacteria and phage are one of the two species most commonly found in ecology[110-111]. Bacteria are important for microbial world to direct the regulation of ecological balance[112]. Bacteria are in charge of adjusting nitrogen level, produce oxygen for all living creatures[113]. Bacteriophage are types of virus that consume bacteria to maintain their life cycles[114]. Phage-bacteria interaction is very important for solving fundamental ecological problems and for the protection of the balance of nature[115]. The relationship between bacteria and phage is examined in three main life cycles[116]. These are respectively lytic phage, temperate phage (lysogenic) and pseudolysogeny phage cycles[116] as shown in Figure 2.13[117]. Some of these life cycles may be harmful to the bacteria, and some are useful for the bacteria[118].

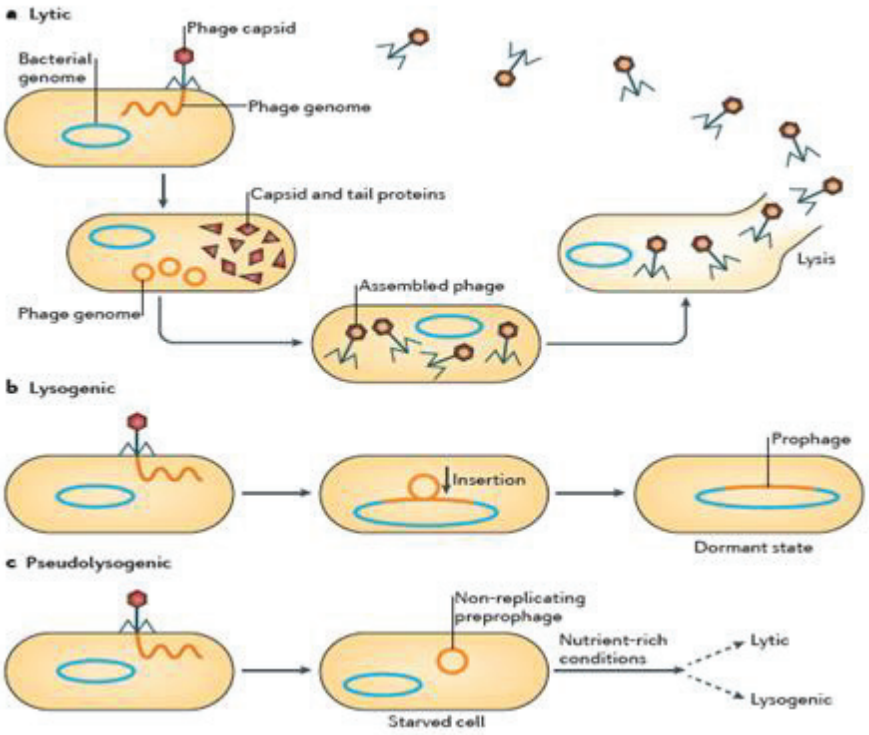

Figure 2.13. Schematic Representation of Interaction of Phage and Bacteri cycles[117]

In lytic cycles, phages attach to the host cells and infect the host cells by leaving their genetic material directly in host cell[119] or via endocytosis mechanisms[120]. It is necessary to recognize bacterial receptors such as lipopolysaccharides[121] and flagella[122] for the phages to bind the bacteria. After binding to the phage host cell, the cell phage will produce nucleic acid-encoded proteins and the phage replicate the genetic material. Then the proteins of the phage take their genetic material into the capsid[123]. After a sufficient number of phages are generated, the phages kill the host cell and this process continues until a new host cell is found[124]. In the lysogenic cycle, the phages have ability to combine their genetic material with the bacterial genome called prophages. Also phage can transfer their genomes to the daughter cell during the growth of the bacteria[125]. When the phages encounter difficult conditions, the phages enter the lytic cycle again, and kill the cell[126]. Many prophages have useful effects on host cells such as increasing the strength of host cells to cope with challenging conditions[127].

The pseudolysogeny life cycle is interpreted differently among researchers[128], but the most accepted interpretation of the pseudolysogeny life cycle is that the phage does not prefer to combine their the genetic material with host cell or does not accept enter the

lytic life cycle[129-130]. This situation is related to the nutritional insufficiency of cell[131]. However, it is not known exactly whether this life cycle is a true life cycle[132].

CHAPTER 3

EXPERIMENTAL

The experimental section includes the design of the mechanical and electronic parts of the LSPR spectroscopy and the biological applications of the LSPR device as a potential biosensor.

3.1.Construction of Localized Surface Plasmon Resonance Spectroscopy

The construction process of LSPR spectroscopy consists of mainly two parts: construction of mechanical and electronic parts. These are explained in detail in the following sections.

3.1.1.Construction of Mechanic System

Mechanical system of the device is composed of five parts designed using three dimensional drawing software named Solid Works 2015®. Technical details of device parts are shown in result part. During the production of device mechanical parts computer numerical control machine, generally known as CNC in metal industry, owned by '*Yerli Makina*' settled in Organized Industry Area in Izmir was used. As a raw material, aluminium was chosen because of process ease and low cost.

3.1.2.Construction of Electronic System

The electronic system of the device consists of two parts; a spectrophotometer and a light source. The light source and the spectrophotometer are connected to the first and last parts of the device by fiber optic cables, respectively and both equipments were purchased from the Ocean Optics Company. The spectrophotometer combines a 2-MHz

analog-to-digital (A/D) converter, programmable electronics, a 2048-element CCD-array detector, and an USB 2.0 port yielding high spectral response and high optical resolution. Also, it has a UV-sensitive coating that makes the system versatile enough for working with UV-Vis light. The spectrophotometer allows the capture and storage of a full spectrum into memory every millisecond enabling observations to be made within 0,1 nm wavelength. The spectrophotometer appears to be convenient for using in the fields of chemistry, biotechnology and other related fields. The spectrophotometer is linked to a computer via the USB port and controlled by Spectra Suit software®, created by Java programming language. Detailed information about the spectrometer is listed in Table 3.1.

Table 3.1. Properties of Spectrophotometer used in LSPR Device

PHYSICAL	**DETECTOR**	**SPECTROSCOPIC**	**ELECTRONICS**
Dimensions: 89.1 mm x 63.3 mm x 34.4 mm	Detector:Sony ILX511B (2048-CCD array)	Optical Resolution: 0.1-10.0 nm FWHM (configuration dependent)	Power Consumption: 250 mA @ 5 VDC
Weight: 190 gr	Detector Range: 200-1100 nm	Signal-to-Noise Ratio:250:1(Full signal)	Connector: 22-pin connector
	Pixels: 2048 pixels	A/D resolution: 16 bit	
	Pixel Size: 14 µm x 200 µm	Dark noise: 50 RMS counts	
	Pixel Well Depth: 62,500 electrons	Dynamic range:8.5 x 10^7 (system); 1300:1 for a single acquisition	
		Integration Time: 1 ms – 65 seconds	
		Stray Light:<0.05% at 600 nm; <0.10% at 435 nm	
		Corrected Linearity: >99%	

The second part of the electronic system is the light source which offers stable, continuous output between 215 nm and 2500 nm. Using tungsten-halogen lamps, light source is ideal for measuring a sample that has multiple features in different spectral regions or for analyzing a variety of different samples. Specifications of light source are shown in table 3.2.

Table 3.2. Features of Light Source used in LSPR Device

Sources	**Deep-UV Deuterium & Tungsten Halogen**
Wavelength Range	190-2500 nm
Warm-up Time	25 minutes
Source Lifetime	1,000 hours
Operating Temperature	5 °C – 35 °C
Power Requirements	85-264 V, 50/60 Hz
Dimensions (W x H x L)	15 x 13.5 x 28.5 cm
Weight	5 kg

3.2.Synthesis and Functionalization of Gold Nanorod

3.2.1.Materials

Cethyltrimethylamonium bromide (CTAB) - Sigma, L-Ascorbic acid - Fluka, TetraChloroauric acid ($HAuCI_4$) and Silver nitrate ($AgNO_3$) - Alfa Aesar, Sodium Borohydrate ($NaBH_4$) - Sigma, N-ethyl-N'-(3-dimethylaminopropyl) carbodiimide hydrochloride (EDC) – Merck, N-Hydroxysulfosuccinimide (Sulfo-NHS) – Thermo , Methoxy-Polyethylene glycol (mPEG-SH, MW 5000) – Laysan Bio, Thiol- and amine-bifunctional PEG (SH-PEG-NH_2, MW 5000) Biochempeg, Potassium Carbonate – Sigma, (3-Mercaptopropyl)trimethoxysilane (MPTMS). 2-keto 3-Deoxy-D-glycero-D-galacto-2-nonulosonic acid (KDN) – Sigma, Citric Acid – Sigma. All chemicals were used as received. Anti-KDN monoclonal antibody was kindly provided by Prof. Dr. Gülperi Öktem at Ege University.

3.2.2.Fabrication of Gold Nanorods via Seed Mediated Method

3.2.3.Preparation of Seed Solution

$HAuCl_4$ in DI water was added into aqueous CTAB solution under magnetic stirring. Ice-cold $NaBH_4$ solution in DI water was added to the mixture. The color of the solution turned into brownish color within seconds. Afterwards, seed solution was kept at 30 ^{0}C for two hours in order to remove free Na ions[133].

3.2.4.Preparation of Growth Solution

CTAB solution in DI water and $HAuCl_4$ solution in DI water were mixed under magnetic stirring $AgNO_3$ solution in DI water was added to this mixture. After addition of ascorbic acid as a mild reducing agent, the color of the solution immediately turned into colorless. Finally, seed solution was added. The solution was stirred for 30 minutes. Approximately 10 minutes later, the color of the growth solution changed according to the size. Gold nanorods were kept in dark for further use[133]. Silver nitrate concentration was changed to produce gold nanorods in different aspect ratios.

3.2.5.Surface Modification of Gold Nanorods

Surface modification of gold nanorods was carried out using bi- and mono-functional PEG molecule mixture. To replace CTAB molecules on the surface of gold nanorods with a mixture of bi- and mono-functional PEG molecules, i.e. monomethoxy-PEG-thiol (mPEG-SH) and amine-PEG-thiol (NH_2-PEG-SH), gold nanorods were first centrifuged at 12000 rpm for 15 minutes, twice to reduce the CTAB concentration in solution. Mixed PEG solution (NH_2-PEG-SH/ mPEG-SH) in DI water was prepared at varying mPEG-SH: NH_2-PEG- SH molar ratios (1:1, 4:1 and 9:1). The concentration of mixed PEG solution was 1.00 mM. Then the mixed PEG solution (1.00 ml) was added to gold nanorod solution (4.00 ml).

The final solution was magnetically stirred for 30 minutes and left in dark overnight. The next day, the mixture was centrifuged at 12000 rpm for 15 minutes twice to eliminate unbounded PEG molecules[134].

3.2.6.Conjugation of Monoclonal Antibodies to Gold Nanorods

Conjugation method carried out for attachment of anti-KDN monoclonal antibodies to GNR surface is as follow: EDC was used as a crosslinking agent to form active ester of carboxylate groups on monoclonal antibody by means of Sulfo-NHS selectively reactive with amine groups on target molecule. Monoclonal antibody was firstly added in EDC solution in PB buffer at 7.4 (40 mM, 100 μl), then sulfo-NHS solution in PB buffer at 7.4 (7 mg/100 μl) were added into mixture of EDC and antibody to activate the carboxylic groups antibody. The mixture was allowed to react for 15 minutes. Afterwards, PEG coated gold nanorods was added to the mixture. The reaction was continued at +4 ^{0}C overnight. Next day, anti-KDN conjugated gold nanorods solution was centrifuged at 1200 rpm for 15 minutes and then washed with water twice in order to remove the unreacted agents and side-products[135].

3.2.7.Conjugation of Anti-KDN Monoclonal Antibodies to KDN

Antigen-antibody conjugation method was conducted for binding of anti-KDN monoclonal antibodies to their specific antigen 2-keto 3-Deoxy-D-glycero-D-galacto-2-nonulosonic acid (KDN) molecules. The procedure for binding the KDN molecule to the antibody is briefly as follows: The KDN molecule was prepared at 1.5 and 10 mM concentrations in PB buffer (pH:7.4). Antibody-bound gold nanorods were equally placed in three separate tubes. Each tube was added KDN molecule prepared at different concentrations. Then, the KDN molecule was incubated for 1 hour to bind to the antibody. After incubation, the tubes were centrifuged at 12000 rpm for 5 min to remove excess KDN.

3.2.8.Control Experiment of Antibody-Antigen Interaction

The control experiment was performed to show the specificity of the antigen to antibody. Citric acid was used instead of the KDN molecule in the control experiment. The procedure for binding citric acid to antibody-bound gold nanorods is as follows:

The citric acid was prepared at 1.5 and 10 mM concentrations in PB buffer (pH:7.4). Antibody-bound gold nanorods were equally placed in three separate tubes. Each tube was added citric acid prepared at different concentrations. Then, citric acid was incubated for 1 hour. After incubation, the tubes were centrifuged at 12000 rpm for 5 min.

3.3.Detection of Bacteria by LSPR

To further show the potential of LSPR device as a potential biosensor, three different bacteria were used with their specific bacteriophages. Experimental procedure consisted of mainly three steps. First step was to create sensor surface using AuNPs to take signal from the surface. Second step was to prepare three different bacterical cultures on sensor surface. Last step was to detect specific bacteriophages. Procedure for each step is explained in subsections.

3.3.1.Synthesis of AuNPs

AuNPs was produced using classical method. Procedure as follow: 5 mL 0.2 M CTAB solution was prepared in DI water. 0.001 M 2.5 mL $HAuCI_4$ solution was added into the CTAB solution. Then, 600 μL-10 mM ice-cold aqueous solution of $NaBH_4$, was added mixture of CTAB- $HAuCI_4$ under vigorous stirring to form the AuNPs. Note that these nanoparticles carrying CTAB on their surfaces were used as seed in the preparation of gold nanorods as described above, and/or they were simply aged about 20-30 days in dark at room temperature in closed caped vials for maturation and to reach the desired size. They were stored at room temperature until use.

3.3.2.Manufacturing of Sensor Surface

Procedure of making a sensor surface includes substrate preparation and nanoparticles deposition.

3.3.3.Substrate Preparation

Making a sensor platform involved depositing nanoparticles onto the functionalized glass surface via electrical charge interactions and covalent bonding. Before deposition of nanoparticles on glass surface, glass slides have to be washed to remove residues from surface. Washing procedure was done as follows; Glass substrates were immersed in a piranha solution (3:1 30% H_2SO_4: H_2O_2**)** at 65ºC for 0.5 h. Substrates were cooled down at room temperature, the glass substrates were rinsed thoroughly with DI water and then sonicated for 60 minutes in 5:1:1 H_2O:NH_4OH:30% H_2O_2. The substrates were rinsed repeatedly with copious amounts of water.

3.3.4.Nanoparticle Deposition on Substrate

To absorb AuNPs on a clean glass surface, we benefited from differences of electrical charge between glass surface and AuNPs. For this purpose, the glass surface was first functionalized with 5 mM mercaptopropyl trimethoxy silane in ethanol and then waited for three hours to bind of AuNPs on glass surface. After that, glass surfaces were washed with ethanol few times to remove the residuals and dried at room temperature. Next, silane coated glass substrate was immersed in gold nanoparticle solution overnight.

3.3.5.Interaction of Nanoparticles with Three types of Bacteria

For the LSPR experiments, fresh bacterial cultures were prepared by incubating overnight at 37^{o}C the samples taken from the stock cultures of the bacteria stored at 4^{o}C. *E.coli, Staphylococcus aureus and Salmonella infantis*) typical bacterial cultures were used. After overnight bacterial growth, sterile centrifugation was applied at room temperature at 5,000 rpm for 10 min.

Bacterial pellets obtained were washed in sterile water and centrifuged for 3 times, then used in further experiments. The initial concentration of all three bacteria was 10^{8} CFU/mL. Bacterial cultures were conjugated with AuNPs. In the conjugation process, bacterial suspensions (5 μL) were dropped onto the sensor platforms, dried in the safety cabinet in about 30 min at room temperature then LSPR spectra were taken.

3.4.Bacteria and Bacteriophage Interactions

Phage emulsions (5 μL) were dropped onto the bacteria adsorbed surfaces and the change of the LSPR peaks were obtained about one hour which is enough time for bacterial infection by the phages and total destruction of their cell structure. Note that at the end of the selected time the surface was gently washed with water and the LSPR data was taken. Phages specific to bacteria (EcP, SaP and SiPh) were tested. The initial concentrations of all these three phages were adjusted to 10^{8} CFU/mL. Also cross phages were tested on each types of bacteria to verify the specificity.

3.5.Characterization Methods

3.5.1.Atomic Force Microscopy (AFM)

A Nanosurf Instrument Multimode Scanning Probe Microscope operating in tapping mode at room temperature in air was used to obtain topographic data. All imaging operations were conducted with 512 x 512 data acquisitions at a various scan speed.

Oxide-sharpened silicon nitride tips with integrated cantilever with a nominal spring constant of 42 N/m were used. These tips have resonance frequencies between 204 and 497 kHz and an effective radius of curvature at the tip of less than 7 nm. AFM images were manipulated by using Scanning Probe Image Processor (SPIP) software.

3.5.2.Scanning Electron Microscopy (SEM)

Electron microscopic images were taken with the FEI Quanta 250 FEG scanning electron microscope equipped with an in-lens secondary-electron detector at operating range 2-10 KV depends on samples charging, which is located within the Materials Research Center of Izmir Institute of Technology.

3.5.3.Zeta Potential

Zeta-potential measurements of nanoparticles with the dynamic light scattering method based on the measurement of the intensity and variation of the light emitted from the small particles in the dilute solution were obtained with a MALVERN Zetasizer Nano ZS instrument.

3.5.4.X-Ray Photoelectron Spectroscopy (XPS)

Elemental analyzes of the prepared samples were performed with Thermo Scientific K-Alpha Surface Analysis model x-ray photoelectron spectroscopy device. The measurements were taken from an area of 400 μm diameter with x-rays produced by Al K Alfa beam source.

CHAPTER 4

RESULTS AND DISCUSSIONS

4.1.Construction of Localized Surface Plasmon Resonance Spectroscopy

The dimensions of the front part of the device are 90 cm width, 60 cm height, 1 mm thickness. Front part is connected to light source by fiber optic cables, providing light input to the system. As shown in Figure 4.1, in order to connect easily the fiber optic cables to the front part, an apparatus having 5 mm diameter was inserted in the middle of the front part. And also, 10 mm diameter screw holes were provided on each side of the front part for mounting the second part easily.

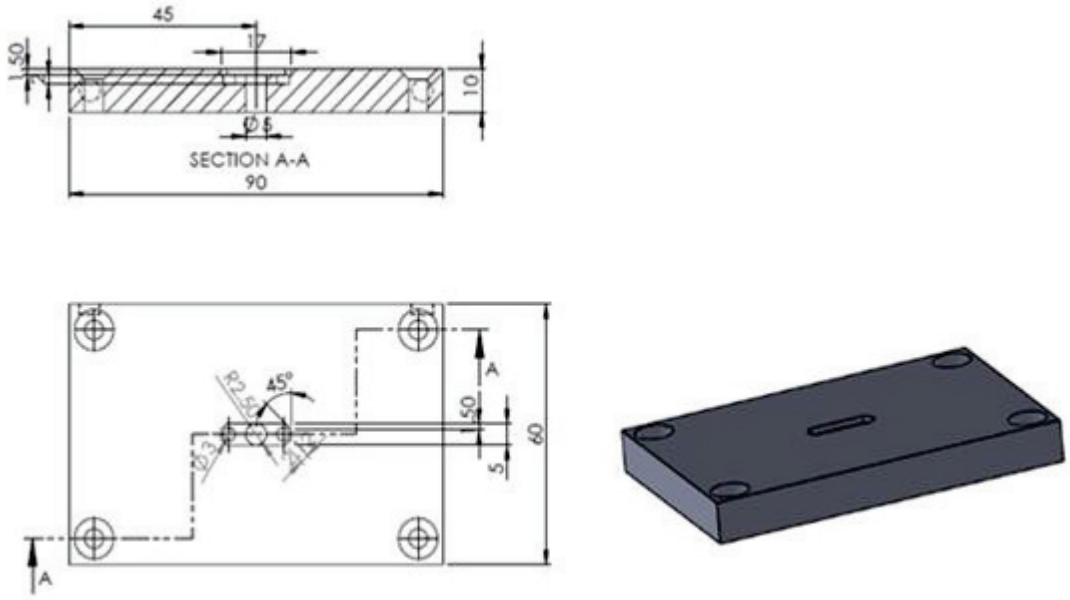

Figure 4.1. Technical drawing of front part of device

The dimensions of the connector part of the device are 90 cm width, 60 cm height, 2 mm thickness. Representative image of connector part is shown in Figure 4.2. This part of the device was designed to facilitate the integration of the microchannel carrier part, which is the main part of the device, into the system. The inside of the connector part

were cut to have a height of 60 cm and a width of 70 cm so that the main part can be placed in the connector part. Holes having a diameter of 10 mm were created to attach the connector part to the back part. To provide sample entry and exit of the microchannels part, channels with a diameter of 1 mm were opened on both lateral surfaces of the connector part. A hole with 5 mm diameter was opened in the middle of the part to allow the passage oflight from the front part to the connector part.

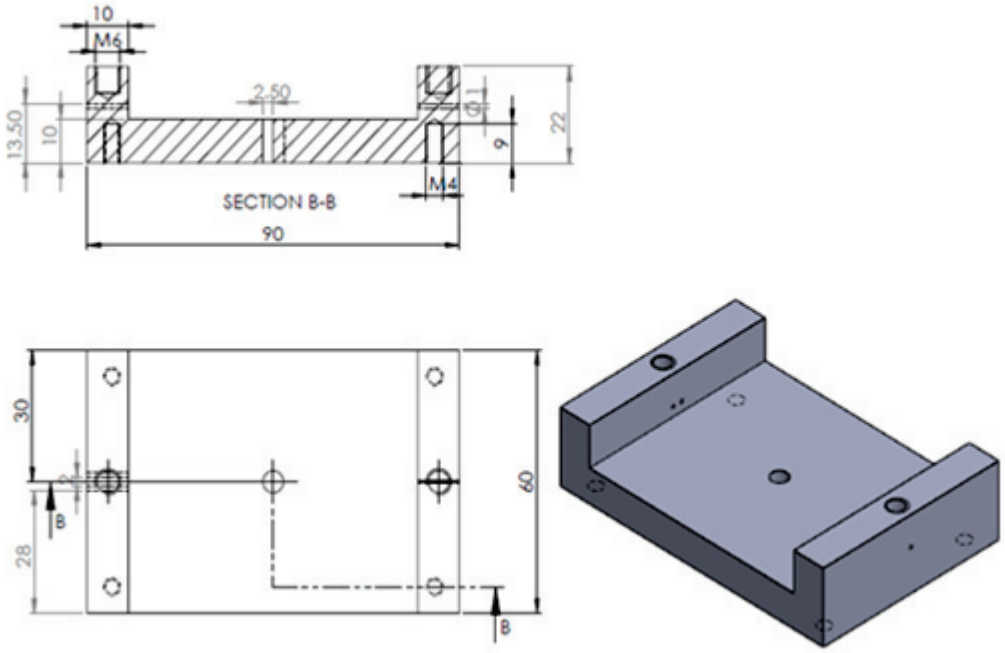

Figure 4.2. Technical drawing of connector of device

In Figure 4.3 shows the microchannel carrier part that can be considered to be the most important part of the device because it is the part at which LSPR based detection events take place. It can be therefore called as the main part of the device. The main part was designed to have a width of of 70 cm and a height of 60 cm high so as to fit the interior of the connector part. An area of 18 mm wide, 42 mm long and 6 mm deep was built in the main part to place microchannels, having two entrances and one exit to observe interactions between the different materials at the same time, in the device. Channels of 1 mm width were formed on both side faces of the main part to deliver the materials to be analyzed in the microchannels. Also, two 3 mm screw holes were drilled to join the fourth part to the region formed for the microchannels. Finally, a hole of 5 mm in diameter was opened in the middle of the main part in order to allow light coming from the front part to reach the detector.

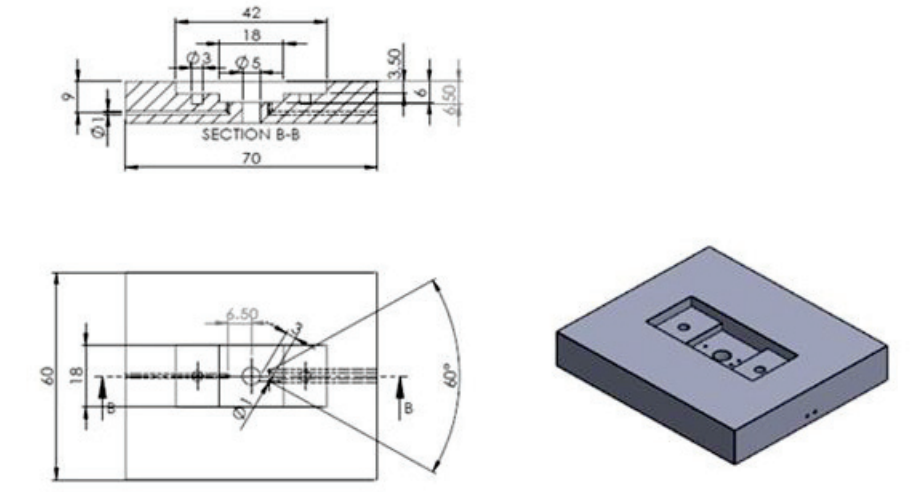

Figure 4.3. Technical drawing of microchannel carrier part of device

The lid of microchannel reservoir is a screw cap system, designed to prevent the leakage of the material to be analyzed through the microchannel, creating pressure between the glass and the microchannel. As shown in Figure 4.4, to be able to generate pressure on the microchannel carrier part, a ring of 15 mm in diameter was placed on the back surface of the lid of microchannel reservoir fourth part. As in all parts, a hole of 5 mm in diameter was opened in the middle of the this part so that the light coming from the fiber optic cables connected to the front part can reach the spectrophotometer.

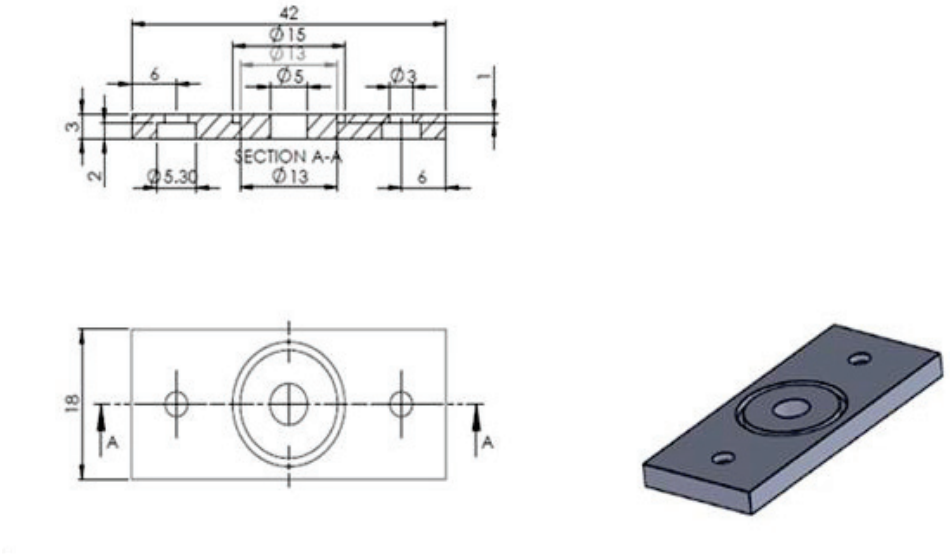

Figure 4.4. Technical drawing of lid of microchannel reservoir

The final part is back part showing in Figure 4.5. The back part that provides the light passing through the system to the spectrophotometer to complete the analysis of the sample. As in the front part, the back part is connected to the spectrophotometer by fiber optic cables and a small apparatus is mounted on the this part to connect the fiber optic cables. The other task of the back part on the system is to fix the location of the main part on the connector part. To achieve this task, screw holes were drilled 10 mm in diameter on both sides of the part.

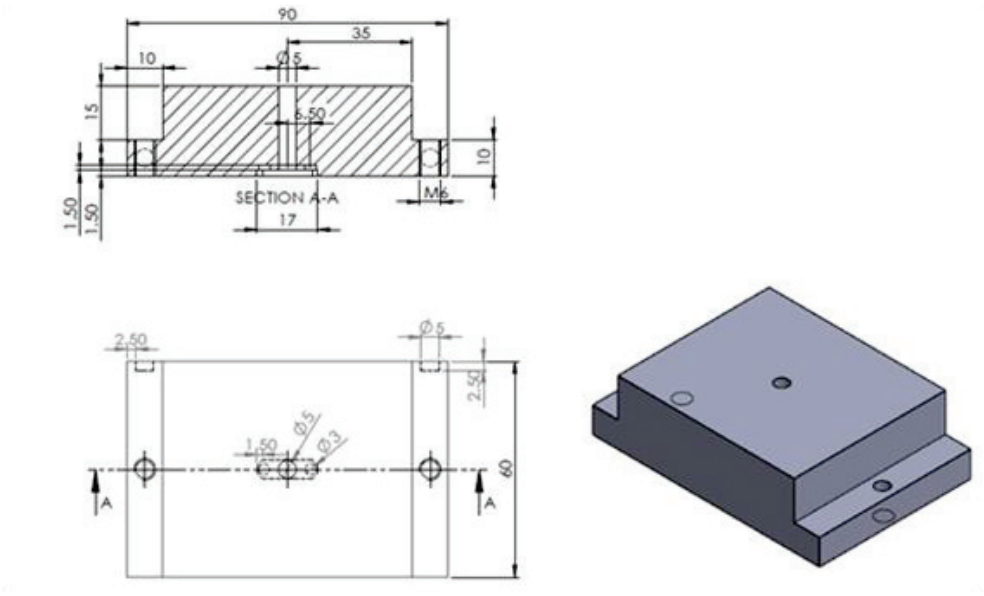

Figure 4.5. Technical drawing of the back part of device

The cartoon image of combination of all parts the device are shown in Figure 4.6. All parts of the device are connected to each other by a screw system. After the completion of technical drawings of the device components, device was produced with the help of computer numerical control machine (CNC) and real image of the final device is displayed in Figure 4.7.

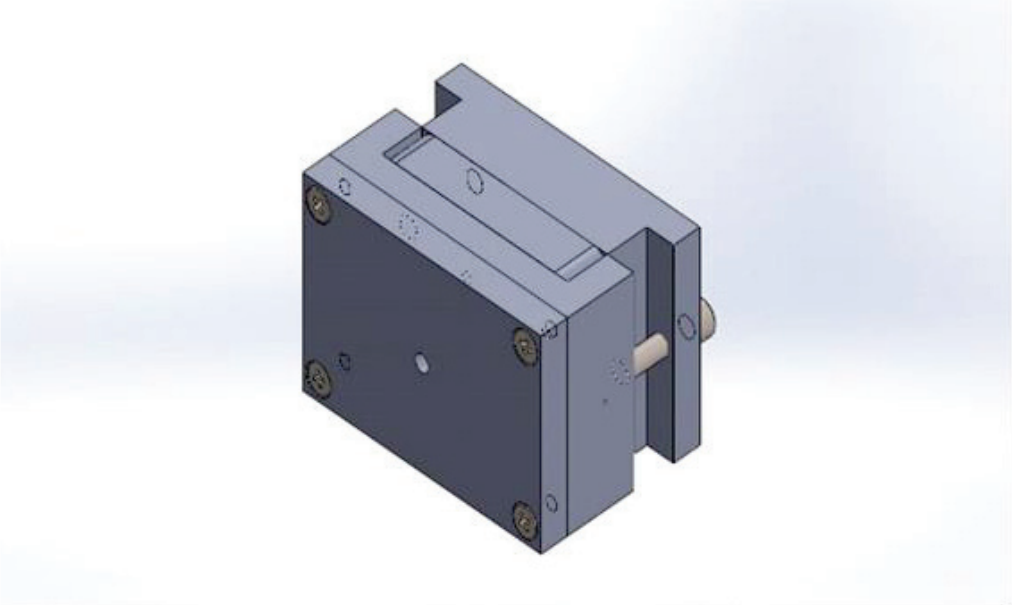

Figure 4.6. Technical drawing of completed device

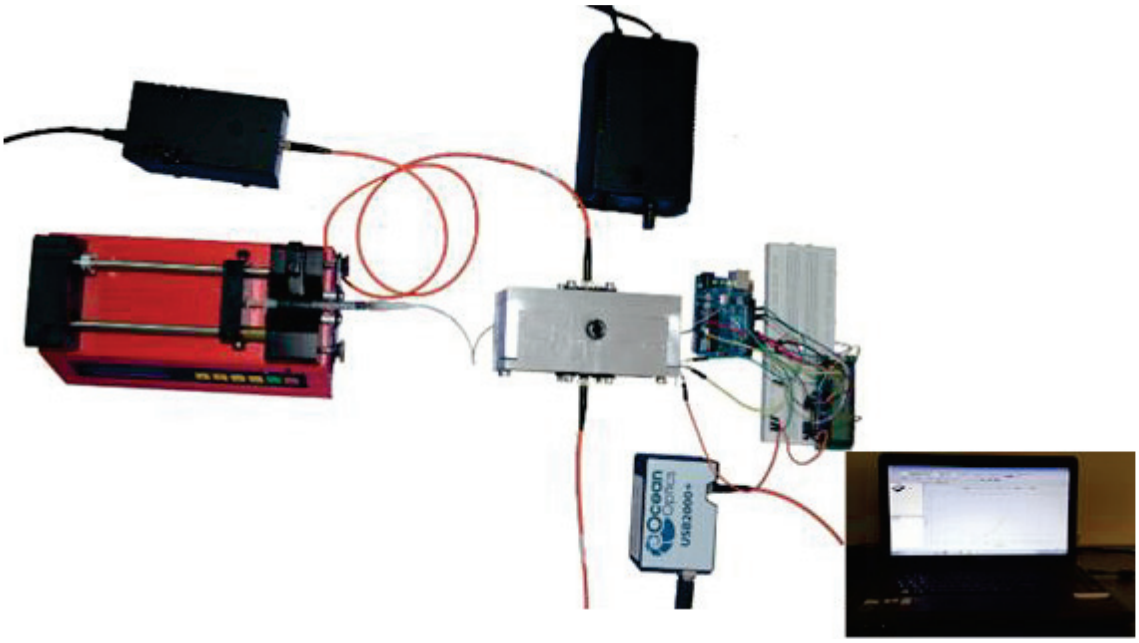

Figure 4.7. Image of the final device

4.2.Synthesis of AuNRs

Green method was applied to produce gold nanorods (AuNRs) at high-yields by varying growth solution composition. AuNRs were produced at high concentrations and certain aspect ratios (30-100 nm in diameter and 10-25 nm in diameter). In Green method, a two-step process involving the synthesis of the seed solution and the growth solution has been utilized. Seed solution was prepared by mixing CTAB as a stabilizer, auric acid as Au source, and sodium borohydride as a reducing agent. . In growth step, the volume ratio of silver nitrate and seed solutions were varied to produce AuNRs with different aspect ratio.

Figure 4.8 displays the LSPR spectrum of AuNRs with varying aspect ratios (2.5, 3.2, 3.8, 4.5),prepared using varying growth medium compositions as explained in the experimental section. AuNRs have two absorption peaks in a specific way. These are transverse absorption peak related to the diameter of the AuNRs, and the longitudinal absorption peak related to the height. The increase in length ratios cause the red shift of the peaks due to the increase in $AgNO_3$ concentration in the growth solution. Changes in the longitudinal plasmon band of the AuNRs are related to the increase in $AgNO_3$ concentration in the growth solution.

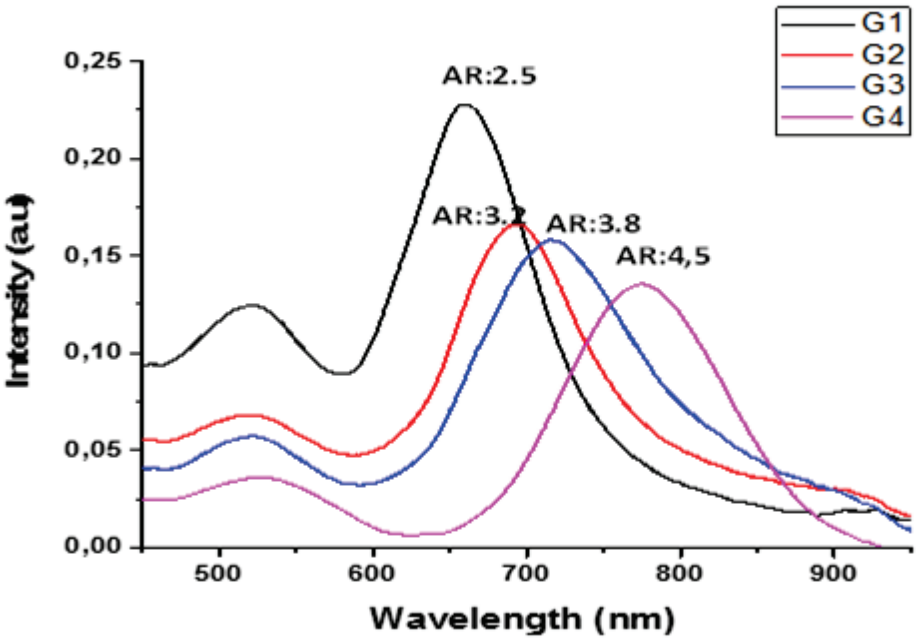

Figure 4.8. LSPR spectra of AuNRs having varying aspect ratios

The transverse plasmon band of the AuNRs synthesized throughout the thesis was observed at approximately 510-520 nm and when the length was increased, the position of the peak did not change. This result indicated that the diameter of the AuNRs synthesized did not change. The second peak, the longitudinal plasmon band, shows the formation and yield of AuNRs. This peak shifted from 650 nm to 785 nm with $AgNO_3$ concentration increase. The amount of red shift of the transverse plasmon band enhances with the increment of length of gold nanorod. LSPR results show that G1 sample (aspect ratio= 2.5) was obtained at the highest yield. The concentration of G1 coded AuNRs sample was measured as 40 ppm using ICP-MS. This highly concentrated sample was used in almost all experiments throughout the thesis.

4.3.Surface Modification of AuNRs with PEG

AuNRs have been used in many biomedical applications such as biosensors, drug delivery and cancer photothermal therapy. The aim of this thesis is to use AuNRs as a platform for biosensor applications.

To effectively use AuNRs in biosensor applications as well as other biomedical applications, AuNRs need to be surface functionalized. In biosensor applications, modifying the surface has some advantages such as reducing toxicity, preventing binding of non-specific proteins, enhancing colloidal stability and incorporating biorecognition ability. AuNRs. The most accepted techniques for functionalizing AuNRs surface include modifying the surface with hydrophilic and nontoxic molecules bearing thiol groups, using layer by layer approach with polyelectrolytes and coating with mesoporous silica.

In this study, thiolated polyethylene glycol (PEG) (Mn 5000 g/mol) was used for modification of AuNRs, because gold has high binding affinity for thiol compounds and thiolated PEG increases colloidal stability of AuNRs and reduces non-specific bindings. The binding of thiolated molecules to the surface of AuNRs leads to a red shift in surface plasmon resonance due to the change of the refractive index of AuNRs surfaces. In the thesis, AuNRs were conjugated with mixtures of mono-functional monomethoxy poly(ethylene glycol)-thiol (mPEG-SH) and heterofunctional amine-PEG-thiol (NH_2-PEG-SH) molecules. Heterofunctional NH_2-PEG-SH molecules were used to create functional sites on the surface for conjugation of antibody. mPEG-SH molecules were

used to form space between NH_2-PEG-SH molecules to allow the efficient binding of antibody molecules. To compare the dose dependent effects of PEG molecules, AuNRs were exposed to two different concentrations (1 mM or 10 mM) of PEG-AuNRs molecules. PEG binding to AuNRs was confirmed by localized surface plasmon resonance (LSPR) spectrometer, zeta potential, scanning electron microscope (SEM), atomic force microscope (AFM) and X-Ray photoelectron spectroscopy (XPS) analysis. Figure 4.9 shows the extinction spectra of AuNRs before and after PEGylation with 1mM and 10 mM PEG mixture.

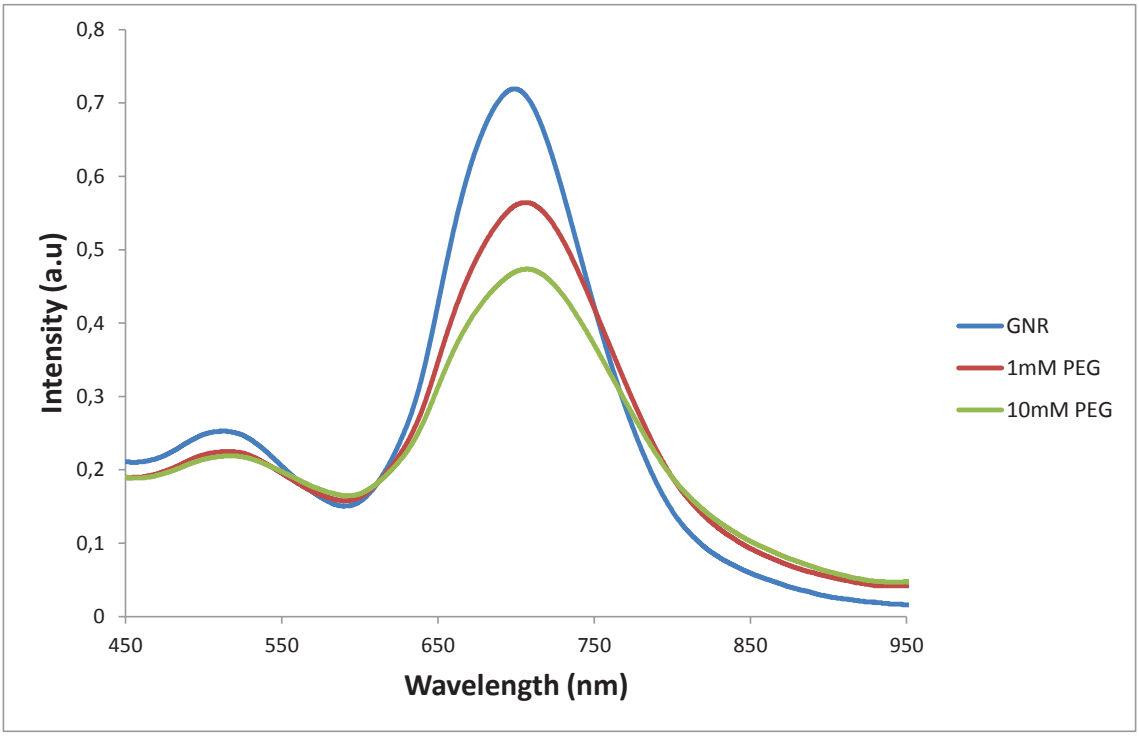

Figure 4.9. LSPR spectra of AuNRs before and after surface functionalization with 1 mM and 10 mM PEG mixture (Molar Ratio of mPEG-SH: NH2-PEG-SH is 4:1)

Figure 4.9 shows the LSPR λ_{max} of the gold nanorod functionalized with PEG mixture at two different concentrations. The LSPR λ_{max} of the bare AuNRs was measured to be 701.24 nm (blue). After AuNRs were incubated with 1 mM mixed polymer solution for 24 hours, he LSPR λ_{max} was measured to be 713.72 nm. An LSPR λ_{max} change of 12.48 nm red-shift was obtained, which was attributed to the binding of polymers (red). When the AuNRs were modified with 10 mM mixed polymer solution for 24 hours, LSPR λ_{max} was measured to be 713.05 nm (green) corresponding to a 12.13 nm red-shift

compared with raw gold nanorod (blue), indicating that the surface was fully saturated with PEG molecules even at 1 mM concentration.

As Figure 4.9 shows, after modifying the AuNRs with PEG molecules at varying concentrations, longitudinal surface plasmon resonance slightly changed towards red region. It was apparently seen that the modification did not remarkably change the optical properties of AuNRs. Decrease in the extinction intensity after modification was visualized suggesting the coating of the surface.

To find optimum conditions for high efficiency antibody binding onto PEG-coated AuNRs, AuNRs were modified with a mixed PEG solution having varying mPEG-SH: NH_2-PEG-SH molar ratios of 1:1, 4:1 and 9:1. Figure 4.10 shows the LSPR spectra before and after AuNRs PEGylation with PEG mixtures having different compositions.

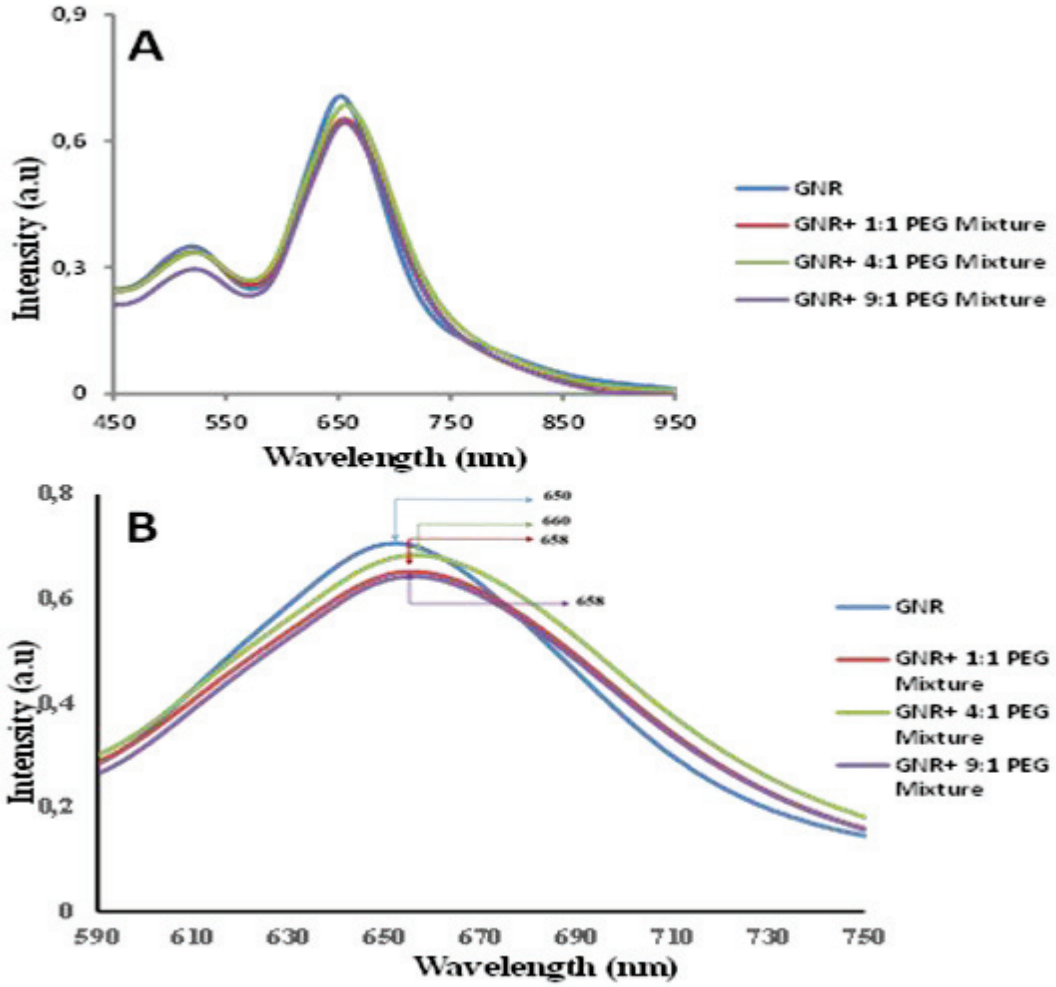

Figure 4.10. LSPR spectra of AuNRs. (A) Unfunctionalized gold nanorods (Blue), after modification with 1:1 PEG Mixture (Red), 4:1 PEG Mixture (Green), and 9:1 PEG Mixture(Purple).(B) Enlarge spectrum of 590 to 750 nm

Figures 4.10A and 4.10B display the LSPR λ_{max} of the AuNRs functionalized with mixed polymers at varying molar ratios. The LSPR λ_{max} of the unfunctionalized AuNRs was measured to be 650 nm (a). AuNRs were incubated with a mPEG-SH: NH_2-PEG-SH mixture of 1:1 molar ratio for 24 hours. After centrifugation of gold nanorod to remove unbounded polymer, the LSPR λ_{max} was measured to be 658 nm. The LSPR λ_{max} change was obtained a 8 nm red-shift that was attributed to the binding of polymers (b). When the AuNRs were modified with a PEG solution of 4:1 ratio, LSPR λ_{max} was measured to be 660 nm corresponding to a 10 nm red-shift compared with unfunctionalized AuNRs (c). Similarly, a 8 nm red-shift compared with unfunctionalized gold nanorod (d) was obtained when a mixed PEG solution of 9:1 ratio was used.

The results show that the optimum molar ratio of PEG mixture 4: 1 molar ratio. The results indicate that the longitudinal plasmon peak changed after functionalization of AuNRs with polymers. In addition, after functionalization, the absence of longitudinal peak expansion is indicative of the fact that the AuNRs functionalized with the PEG mixture do not tend to aggregate in solution. Furthermore, the results displayed that after centrifugation of PEG-AuNRs, the absorption intensity of PEG-AuNRs declined compared to bare AuNRs. The reason for this is that both excess AuNRs and PEG molecules were removed from solution.

The zeta potential of AuNRs was also measured via Malvern Zeta Sizer before and after functionalization AuNRs with mPEG-SH: NH2-PEG-SH mixtures at varying ratios (Table 4.1). Zeta potential of AuNRs was measured to be 11.1 mV prior to functionalization with PEG mixture.

Since CTAB is a cationic molecule, CTAB-stabilized AuNRs showed cationic surface charge. After interaction with the PEG mixture, CTAB molecules predominantly present on the surface AuNRs are replaced by PEG molecules. The interaction of the AuNRs and PEG mixtures at three different mole ratios (mPEG-SH: NH_2-PEG-SH, 1:1; 4:1; 9:1) leads to zeta-potential values shifted from 11.1 mV to -6.64 mV, -8.79 mV, -13.76 mV respectively. Functionalization with the PEG mixture causes the AuNRs to have an anionic surface.

Table 4.1. Zeta potential of AuNRs before and after PEGylation with mPEG-SH and SH-PEG-NH_2 mixtures at varying ratios

Sample	**Zeta Potentials (mV)**
CTAB-GNR	11.1±0.17
PEG MİXTURE (1:1) (mPEG-SH and SH-PEG-NH_2)	-6.64±0.11
PEG MİXTURE (4:1) (mPEG-SH and SH-PEG-NH_2)	-8.79±0.21
PEG MİXTURE (9:1) (mPEG-SH and SH-PEG-NH_2)	-13.76±0.32

Figure 4.11 shows scanning electron microscope (SEM) images of AuNRs before and after functionalization with PEG. Figures 4.11A and 4.11B are SEM images prior to functionalization of AuNRs. From Figures 4.11A and 4.11B, it was observed that AuNRs were locally clustered in some regions. Figures 4.11C and 4.11D show the SEM images after AuNRs functionalization with PEG. The PEG layers around the AuNRs were clearly visible. SEM images also showed that AuNRs were synthesized at high concentration. From the SEM images, the diameter and the length of the AuNRs were calculated to be 14 nm and the length to be 35 nm.

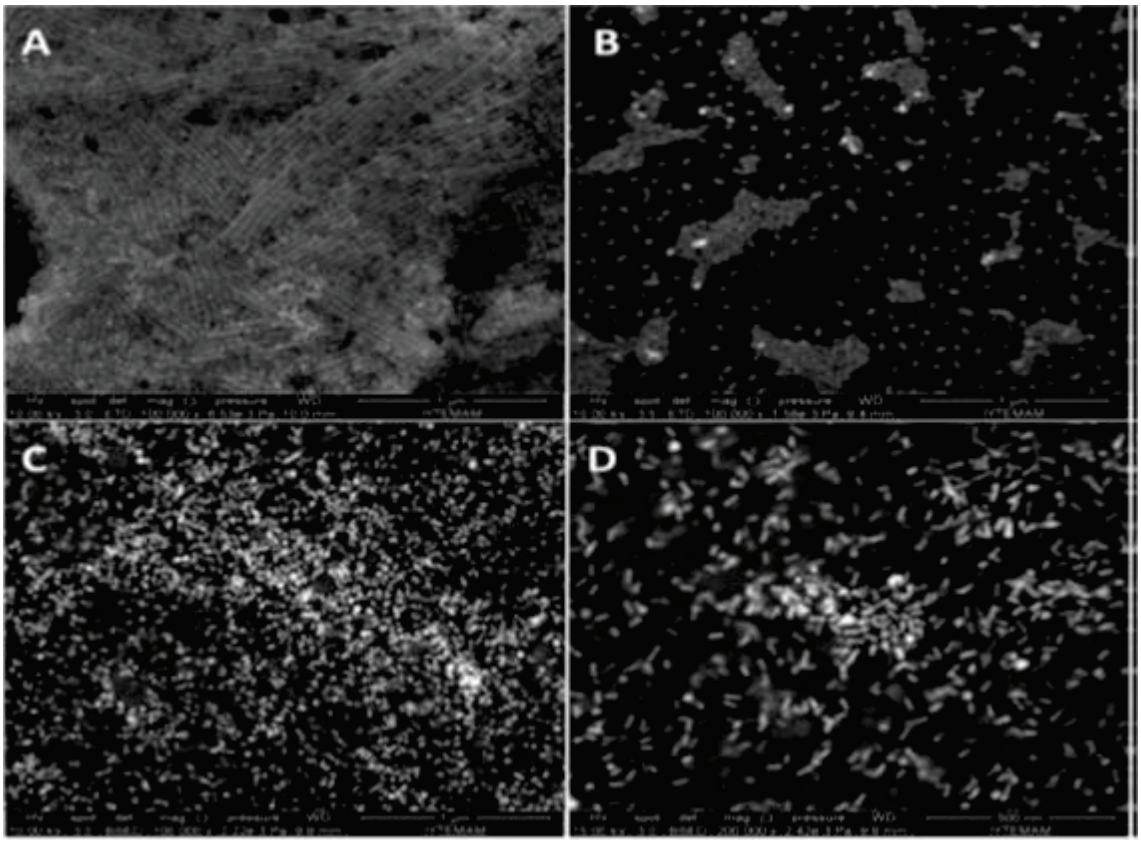

Figure 4.11. SEM images of AuNRs at different magnifications (A-B) before and (C-D) after functionalization AuNRswith PEG mixture

Atomic Force Microscopy images were taken to support the results obtained from the Scanning Electron Microscope. AFM images were taken using the tapping mode before and after AuNRs were functionalized with a mixture of mPEG-SH and NH_2-PEG-SH . In Figure 4.12A, the diameter and length of the AuNRs were calculated to be 20 nm and 48 nm, respectively. Figure 4.12B is a high magnification AFM image of AuNRs. Figures 4.12C and 4.12D are topographical images of AuNRs that are activated with the PEG mixture. Morphology of AuNRs changed after conjugation with PEG. The PEG layer on AuNRs is clearly visible in AFM images. A higher magnification of the image in Figure 4.12C is shown in Figure 4.12D. The length of PEG-bonded AuNRs was found to increase compared to the unbounded AuNRs.

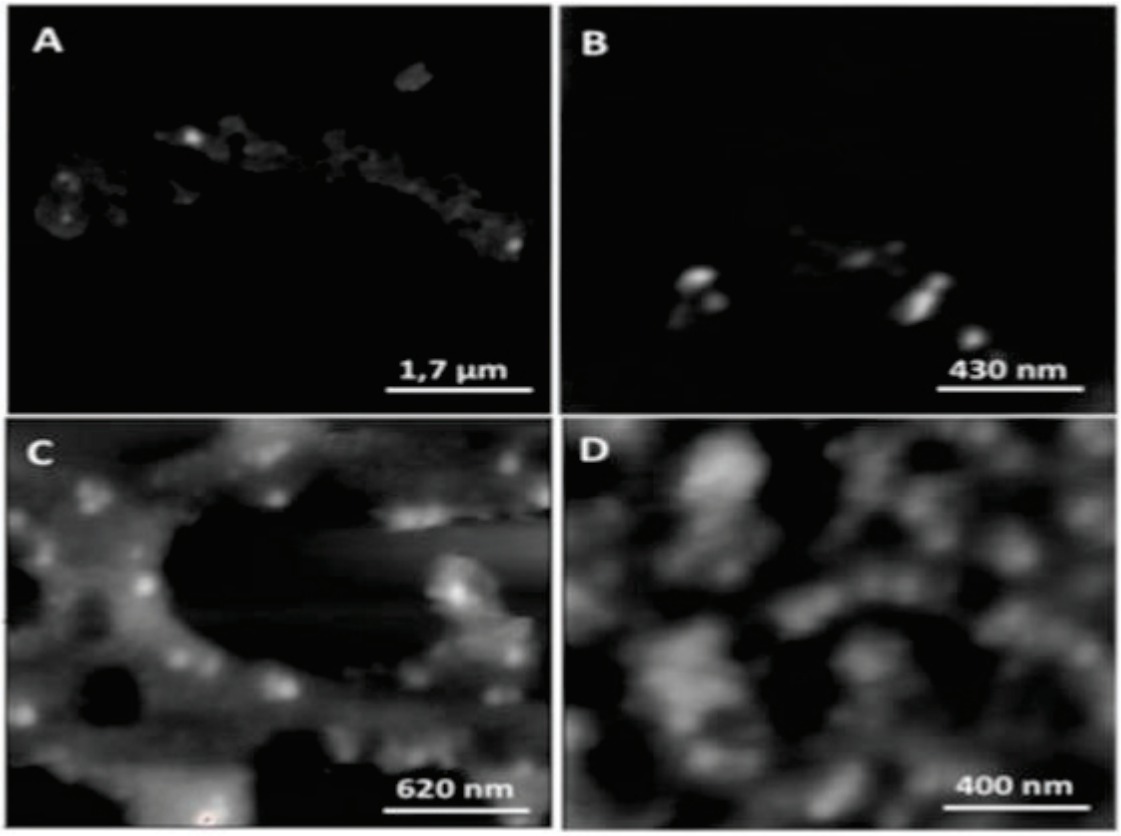

Figure 4.12. Low and high resolution topographical AFM images of AuNRs (A and B) before and (C and D) after PEGylation of AuNRs

In addition to LSPR and zeta analyzes, x-ray photoelectron spectroscopy (XPS) analysis was performed to confirm the surface modification steps of AuNRs. X-ray photoelectron spectroscopy (XPS) is a surface-sensitive quantitative spectroscopic technique that measures the elemental composition in the surface region and chemical state information of the elements. In XPS measurements, bare AuNRs, PEG-AuNRs) and Ab-PEG-AuNRs were examined. The elemental analyses of AuNRs and PEG-AuNRs are shown in Table 4.2. In AuNRs result, most of the elements observed are due to CTAB molecules surrounding the gold nanorods. Silicon and silver elements observed in XPS analysis might be due to substrate and formation of gold nanorod, respectively.

Table 4.2. Elemental composition of AuNRs and PEG-AuNRs in XPS measurement

	AuNRs		*PEG-AuNRs*	
	Peak BE	***Atomic %***	***Peak BE***	***Atomic %***
Br3d	68.01	1.71	-	-
C 1s	285.22	54.70	285.91	74.97
Ag 3d	368.09	0.37	367.90	0.44
N1s	402.42	2.47	-	-
O 1s	532.99	13.58	532.85	21.24
Au4f7	84.16	4.65	84.06	1.09
Si2p	99.92	22.52	-	-
Na1s	-	-	1071.33	1.38
S2p	-	-	167.35	0.90

The elemental percentages of AuNRs and PEG-AuNRs analyzes are also shown in Table 4.3. In these measurements, the S atom of PEG molecules, anchoring with the gold surface has been observed. Besides, the Br atoms of CTAB molecules were not found. These results show that CTAB molecules are replaced by PEG molecules with high efficiency. Due the carbon and oxygen elements present in the PEG molecule, the ratio of carbon to gold and ratio of oxygen to gold increased after binding of PEG on AuNRs.

Table 4.3 Elemental percentages of AuNRs, PEG-AuNRs in XPS measurement

%	AuNRs	PEG-AuNRs
C/Au	11,76	68,78
O/Au	2,92	19,48
N/Au	0,53	-
S/Au	-	0,825
C/O	4,02	3,53
N/O	0,18	-
S/O	-	0,042
C/N	22,14	-
C/S	-	83,3

4.4.Conjugation of Anti-KDN Monoclonal Antibody to AuNRs

2-Keto-3-deoxy-D-glycero-D-galacto-nononic acid (KDN) molecule is a 2,8-linked polysialic acid (polySia) highly expressed in cancer cells. Monoclonal anti-KDN antibodies have been developed to identify a-2,8-linked polySia, (KDN). Bioaffinity binding between anti-KDN antibody and KDN molecules was chosen in this study as a model binding event to be detected by the LSPR device constructed. Monoclonal anti-KDN antibody was therefore conjugated to PEGylated AuNRs via EDC/Sulfo-NHS chemistry. The conjugation of antibody to PEGylated AuNRs was confirmed by localized surface plasmon resonance (LSPR) spectrometry, zeta potential, dynamic light scattering (DLS) and XPS measurements.

Figure 4.13 depicts LSPR λ_{max} of AuNRs after each surface functionalization step. First, the LSPR λ_{max} of PEG functionalized AuNRs was measured to be 660.02 nm. PEG functionalized AuNRs were then modified with Anti-KDN and the LSPR λ_{max} was measured to be 666.96 nm. The LSPR λ_{max} shift corresponding to this surface functionalization step was a 6.94 nm red-shift with regard to PEG functionalized AuNRs. This shift is an expected result because of the binding of antibody and is consistent with literature.

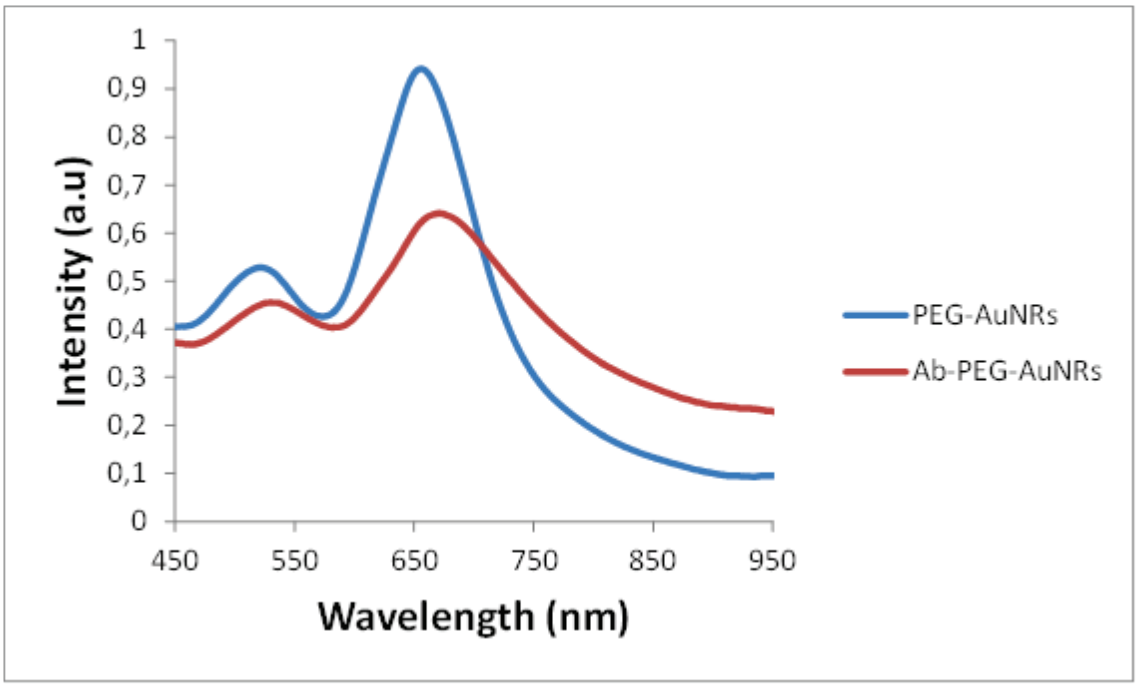

Figure 4.13. LSPR spectra of PEG-AuNRs before (blue) and after (red) conjugation with anti-KDN antibody

The results of zeta potential and dynamic light scattering analyses before and after conjugation with antibody are shown in Table 4.4. The zeta potential of AuNRs, PEG-AuNRs), Ab-PEG-AuNRs was measured. Zeta potential measurement shows changes in surface charge as a result of functionalization processes on AuNRs. The zeta potentials of AuNRs and PEG-AuNRs were 11.1 and -8.79 mV, respectively. After conjugation of anti-KDN antibodies, the zeta potential of the rods was measured to be -1.6 mV.

Table 4.4. Zeta Potential and Size measurements of AuNRs, PEG-AuNRs and Ab-PEG AuNRs

Sample	**Zeta Potential (mV) (PBS)**	**Size (nm) (PBS)**
AuNRs	11.1±0.17	261,3±18,8
PEG-AuNRs	-8.79±0.21	13.2 ±0,06
Ab-PEG-AuNRs	-1.6±0.01	48.7 ±1,7

Antibodies have net positive charge at neutral pH. Theoretically, the zeta potential value is expected to increase after antibody binding to PEG-AuNRs. The increase in the zeta potential of the PEGylated nanorods after antibody conjugation from -8.79 to -1.6 mV was attributed to the fact that the antibody conjugation process took place. It should be noted that in the antibody conjugation experiments no change was observed in the zeta potential values of the control samples which were AuNRs exposed to the same conjugation procedure without using an antibody.

The change in the size of PEG-AuNRs after antibody conjugation was also measured by dynamic light scattering (DLS) and the results are shown in Table 4.4. It is known in the literature that DLS measurements do not show the exact dimensions of the nanorods, but display only an apperant size. Thus by performing DLS experiments, it is aimed to have an idea about the modifications by determining the changes in hydrodynamic sizes depending on the modifications on the surfaces of nanorods. The hydrodynamic size of the PEG-AuNRs was measured as 13.2 nm. This value is in agreement with the width value measured in the SEM image of the nanorods.

After the PEG-AuNRs were interacted with the antibody, the hydrodynamic size was measured as 48.7 nm. Approximately 35 nm increase upon antibody conjugation is in good accord with the size of an antibody given in the literature.

Table 4.5 gives the elemental analysis of PEG-AuNRs and Ab-PEG-AuNRs. Detailed screening was performed for the nitrogen atom in XPS analyzes after antibody conjugation. While nitrogen atoms could not be observed in PEG-AuNRs, they were clearly observed after antibody conjugation. This XPS result showed that antibody molecules containing a large number of nitrogen atoms due to their protein structure present on the surface of AuNRs. Incorporation of high quantity of nitrogen atoms in the composition also reduces the relevant carbon atom percentage as expected. Overall XPS results confirmed the binding of antibody molecules on the AuNRs surface. When analyzing XPS data, the ratio of the atomic percentages of the elements calculated and each conjugation step can interpret. Table 4.6 depicts the percentage ratio of the elements.

Table 4.5. Elemental composition of PEG-AuNRs and Ab-PEG-AuNRs in XPS measurement

	PEG-AuNRs		Ab-PEG-AuNRs	
	Peak (BE)	Atomic %	Peak BE	Atomic %
C 1s	285.91	74.97	286.35	38.50
Ag 3d	367.90	0.44	368.27	1.78
N1s	-	-	400.95	5.04
O 1s	532.85	21.24	533.11	25.29
Au4f7	84.06	1.09	84.34	5.10
Si2p	-	-	100.09	25.49
Na1s	1071.33	1.38	1072.07	0.74
S2p	167.35	0.90	-	-

Table 4.6. Elemental percentages of AuNRs, PEG-AuNRs and Ab-PEG-GNRs in XPS measurement

%	AuNRs	PEG-AuNRs	Ab-PEG-AuNRs
C/Au	11,76	68,78	7,55
O/Au	2,92	19,48	4,95
N/Au	0,53	-	0,988
S/Au	-	0,825	-
C/O	4,02	3,53	1,52
N/O	0,18	-	0,2
S/O	-	0,042	-
C/N	22,14	-	7,64
C/S	-	83,3	-

4.5.Detection of KDN with Ab-PEG-AuNRs Based LSPR

Specific binding of KDN to Ab-PEG-AuNRs was performed in PB buffer (pH: 7.4) using KDN solutions at varying concentrations. KDN binding to nanorods was investigated by LSPR spectrometry and zeta potential measurements as a supporting technique. LSPR analysis in Figure 4.15 showed that the intensity of the spectrum of nanorods decreased and the peak enlarged after KDN binding. After binding of antibody conjugated AuNRs with increasing concentrations of KDN (1, 5 and 10 mM), the peak wavelength shifted from 665 nm to 668, 669 and 669 nm, respectively. From the results, the antibody-antigen interaction reached saturation between 1 mM and 5 mM KDN

concentration. Also Figure 4.14 shows control experiment of conjugation of PEG-AuNRs with KDN that KDN is only specific for anti-KDN.

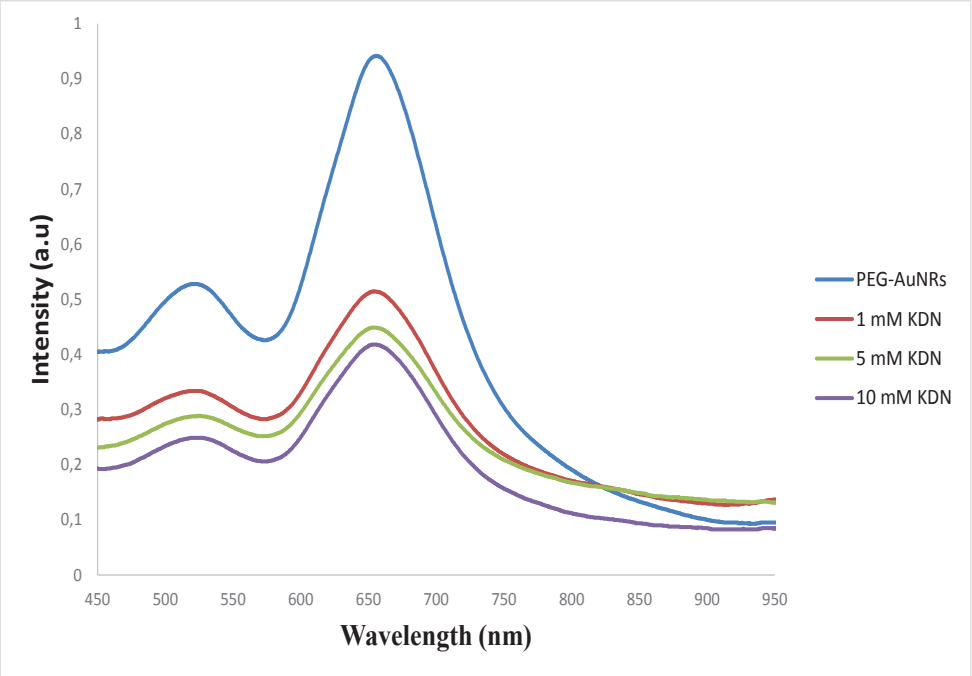

Figure 4.14. LSPR spectra measured after interaction of PEG-AuNRS with KDN solution at varying concentrations

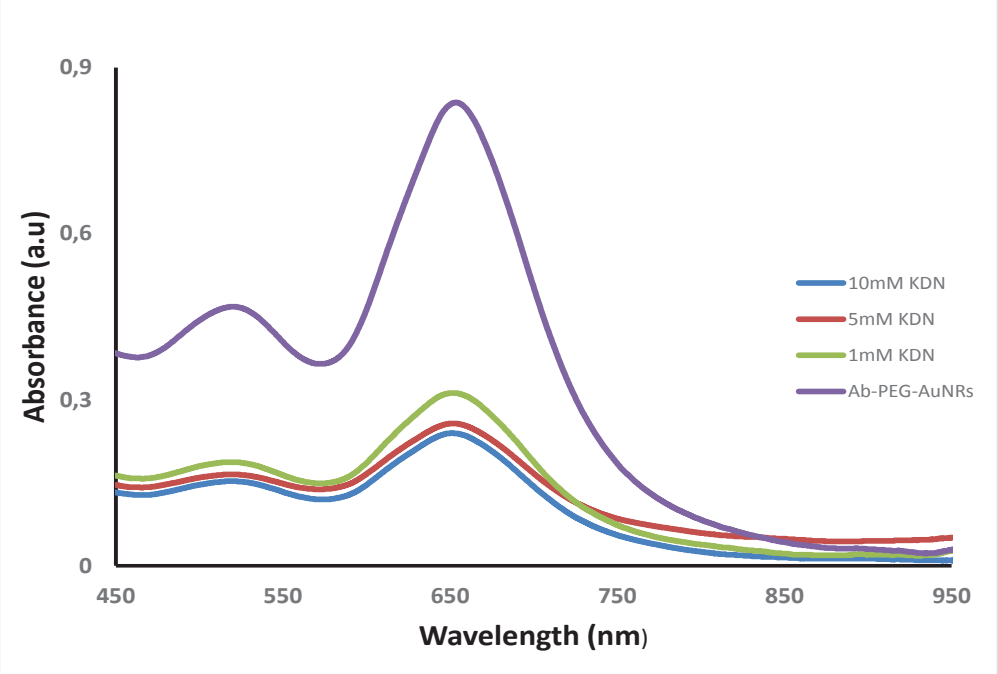

Figure 4.15. LSPR spectra measured after interaction of antibody-bound gold nanorods with KDN solution at varying concentrations

After interaction of Ab-PEG-AuNRs with KDN, zeta potential values decreased from -1.6 to -14.2, -15.9 and -19.6 mV, respectively, with increasing KDN concentrations (Table 4.7). According to the results, there is a decrease in zeta potential from a lower KDN concentration to a higher KDN concentration. The KDN molecule is a sialic acid derivative and is an anionic molecule in neutral conditions. The chemical structure of the KDN molecule is shown in Figure 4.16. Thus it is expected that the nanorod surface charge decreases upon binding of KDN molecules to antibodies conjugated to the nanorod surface.

Table 4.7. Zeta potential values of Ab-PEG-AuNRs before and after interaction with KDN at varying concentrations

Sample	**Zeta Potential (mV)**
Ab-PEG-AuNRs	-1.6±0,01
Ab-PEG-AuNRs +1 mM KDN	-14,2±0,46
Ab-PEG-AuNRs +5 mM KDN	-15.9±1,45
Ab-PEG-AuNRs +10 mM KDN	-19.6±0,20

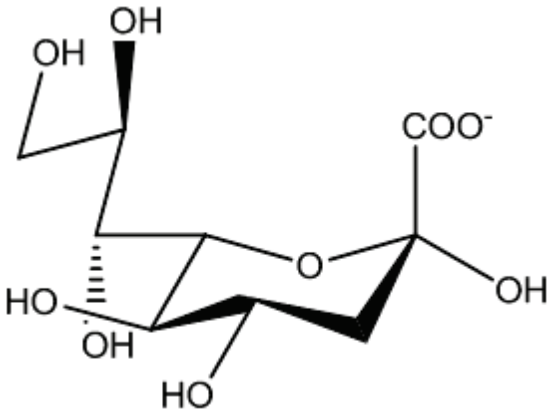

Figure 4.16. Chemical structure of 2-Keto-3-deoxy-D-glycero-D-galacto-nononic acid

At 1 mM concentration of KDN, due to its affinity binding to antibody-conjugated surface, the surface charge of the nanorods significantly decreased to negative (from -1.6 to -14.2). Increasing the KDN concentration makes the surface potential more negative, but the change in surface potential is small at high concentrations (for 5 mM:-15.9, 10 mM: -19.6), possibly due to reaching saturation point or non-specific bindings Zeta potential values support the LSPR results.

4.6.Control Experiment of Antibody-Antigen Interaction

As a control experiment, citric acid was used instead of KDN to investigate whether the binding events observed between KDN and anti-KDN antibody coated AuNRs were not due to electrostatic or non-specific interactions. When citric acid, an anionic small molecule, solution was introduced to Ab-PEG-AuNRs based LSPR system. Similar to KDN, citric acid was used at concentrations of 1, 5 and 10 mM. Each functionalization step was analyzed via LSPR. LSPR analysis showed no red shift after incubation of Ab-PEG-AuNRs with citric acid solutions at varied concentrations (Figure 4.17). In each step, the peak wavelength was measured to be 667 nm, however the intensity of the spectrum of nanorods decreased. Since the nanorods are centrifuged after conjugation with citric acid.

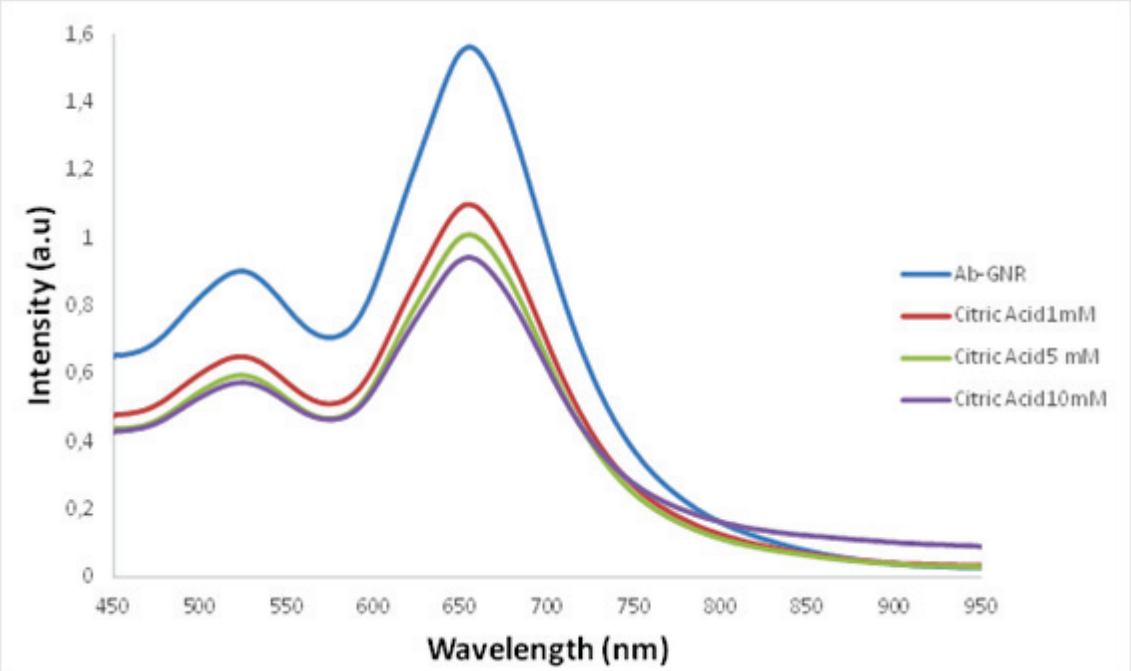

Figure 4.17. LSPR spectra measured after interaction of antibody-bound gold nanorods with citric acid solution at varying concentrations

The zeta potential of Ab-PEG-AuNRs were measured after the citric acid interaction at varying concentrations and the results are shown in Table 4.8. After interaction of antibody conjugated nanorods with citric acid, zeta potential values did not change due to the fact that binding event of citric acid on gold nanorods was not occurred. The zeta potential values are respectively, -5.76 to -5.2, -4.9 and -5.9.

According to the results obtained, no change in zeta potentials indicates that citric acid did not bind the surface of Ab-PEG-AuNRs. The zeta potential results support the LSPR analysis results. Thus the result of the control experiment clearly suggests that the binding of KDN to antibody conjugated PEG-AuNRs is through specific affinity and not through electrostatic interactions.

Table 4.8. Zeta potential values of Ab-PEG-AuNRs before and after interaction with citric acid at varying concentrations

Sample	**Zeta Potentials (mV) (PBS)**
Ab-PEG-AuNRs	-5.76±0,01
Ab-PEG-AuNRs +1 mM Citric Acid	-5,2±0,46
Ab-PEG-AuNRs +5 mM Citric Acid	-4.9±1,45
Ab-PEG-AuNRs +10 mM Citric Acid	-5.9±1,45

4.7.Gold Nanoparticle Based LSPR System For Detection of Bacteria

In this part of the thesis, an alternative nanobased system using bacteriophages as specific bioprobes and nanoparticles was intended to be developed for detection of pathogenic bacteria. Three pathogenic bacteria, *Escherichia coli (E.coli), Staphylococcus aureus* (*S.aureus*) and *Salmonella infantis* (*S.infantis*) were selected as the targets. AuNPs were used to enhance the signals in the detection system based on LSPR spectroscopy. Briefly, LSPR studies were carried out on glass slides modified by deposition of AuNPs. Following the exposure of target bacteria to the surface, LSPR data were collected and the specific phage was added on the bacteria coated surface to determine the type of bacteria. In addition, cross phage reaction in each step was applied as control to demonstrate the specificity.

4.7.1.Synthesis of AuNPs

AuNPs with positive surfaces charges (carrying CTAB on their surfaces) were synthesized by using a seed solution as described in materials and methods section. Figure 4.18 displays the LSPR spectrum of AuNPs synthesized. AuNPs have one absorption peak in a specific way. This is transverse absorption peak approximately at 526 nm, which corresponds to the average radius of colloidal AuNPs about 16-20 nm. In addition, SEM image of AuNPs is displayed in Figure 4.19.

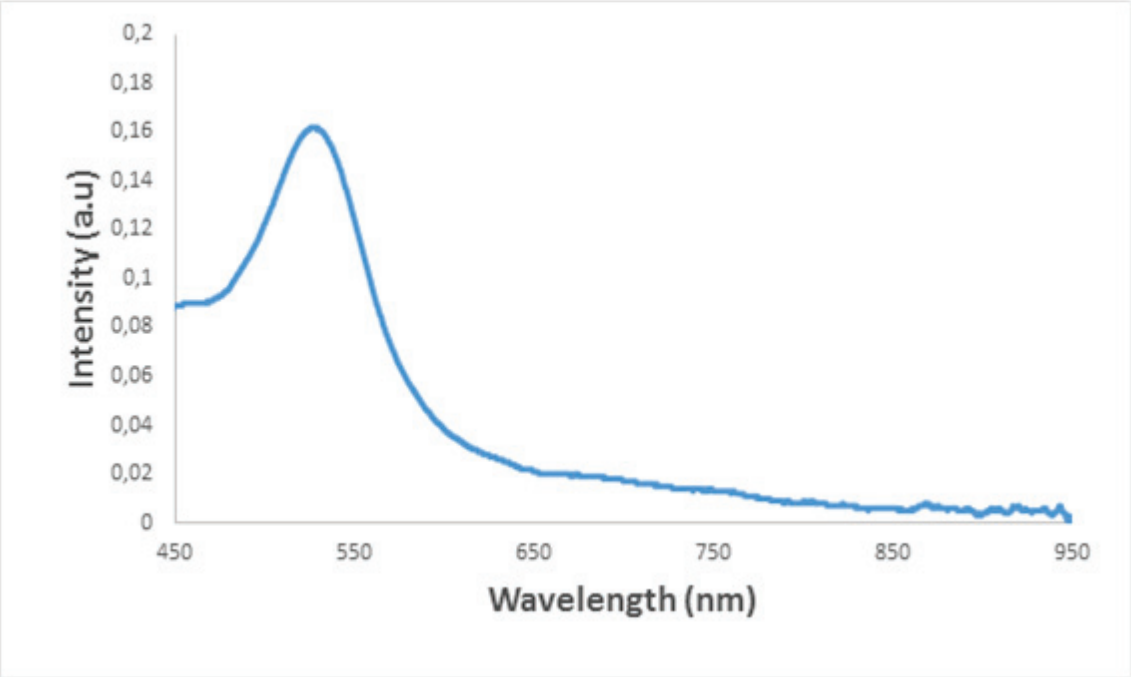

Figure 4.18. LSPR spectra of Gold Nanoparticles (AuNPs)

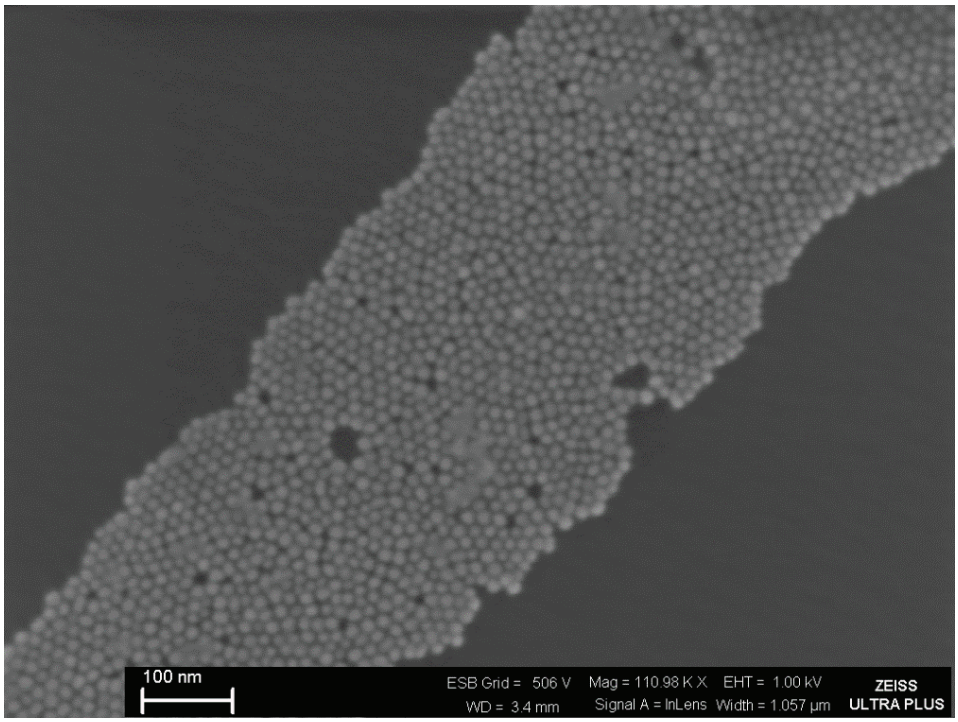

Figure 4.19. SEM image of AuNPs

4.7.2.Modification of AuNPs with *Bacteria and Recognition through Bacteriophages*

The AuNPs were modified with *E.coli*. Thespecific phage of the E.coli namely, T4 was then added on the E.coli coated AuNPs. In the last step of this section, specific phage of Salmonella namely, SaP was added to prove the specificity of the T4 phage towards E. coli. LSPR measurements were performed at each step (Figure 4.20).

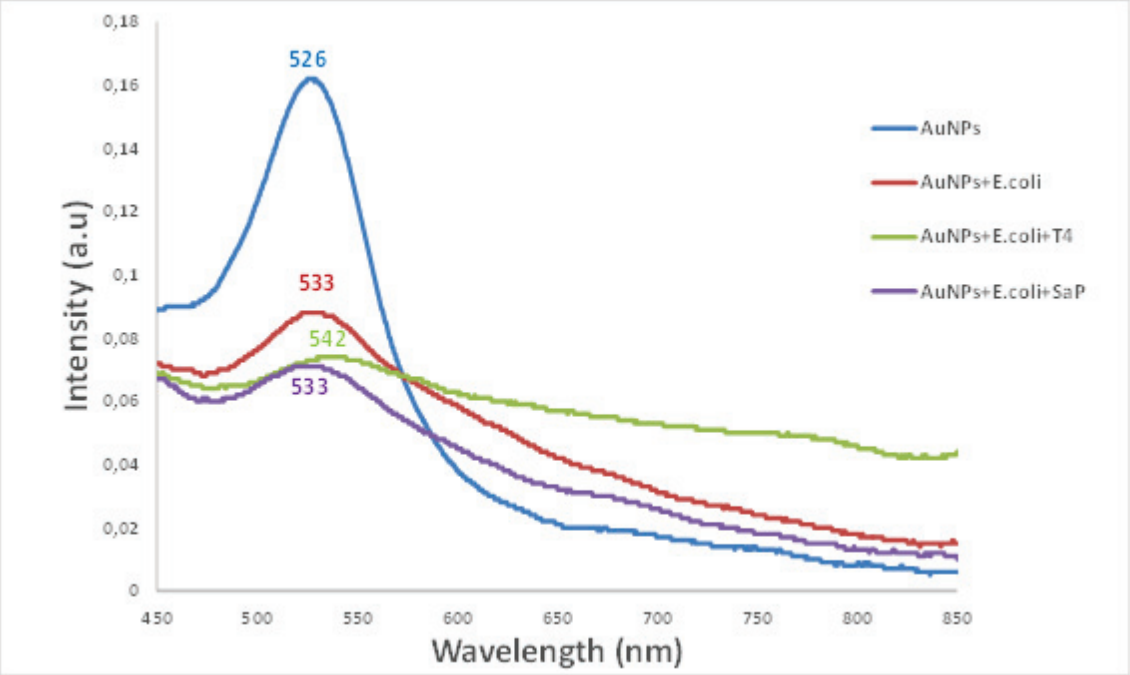

Figure 4.20. LSPR analysis of *E.coli* modified AuNPs and T4 bacteriophage interaction AuNPs (Blue), AuNPs modified with *E.coli* (Red), Bacteriophage (T4) Interaction with *E.coli* modified AuNPs (Green), Salmonella phage (SaP) Interaction with *E.coli* modified AuNPs (purple)

Figure 4.20 displays the LSPR λ_{max} of conjugation process of AuNPs with *E.coli*. The LSPR λmax of the unfunctionalized AuNPs was measured to be 526 nm. AuNPs were incubated with *E.coli* for 1 hour. After washing of excess *E.coli* on AuNPs, the LSPR λmax was measured to be 533 nm. The LSPR λ_{max} change was obtained an 8 nm red-shift that was attributed to attaching of bacteria to gold surface. *E.coli* attaches AuNPs through electrostatic interactions since AuNPs have positive charge while *E.coli* is a gram negative bacteria and have an outer covering of phospholipids and lipopolysaccharides imparting a strongly negative charge to the surface of bacterial cell wall. AuNPs coated with bacteria were then interacted with specific phage of *E.coli* (T4) for 30 minutes and after that washing step was applied to remove unbounded phage. LSPR λ_{max} was measured to be 542 nm corresponding to a 9 nm red-shift compared with bacteria coated AuNPs. Separately, in order to show specificity of T4 phage towards *E.coli*, bacteria coated surface was also incubated with phage of salmonella. LSPR λ_{max} was measured to be 533 nm. The results showed that *E.coli* was selectively detected with its own specific phage using AuNPs based LSPR system. Because, the LSPR signal did not shift when the phage of the salmonella was added on the *E.coli* modified AuNPs.

The same procedures were also applied for *Salmonella infantis* bacteria and its specific phage namely, SaP. In the control experiment to verify the specifity, T4 phage was used. Figure 4.21 displays LSPR spectra of bacteria and bacteriophage interactions for *Salmonella infantis*.

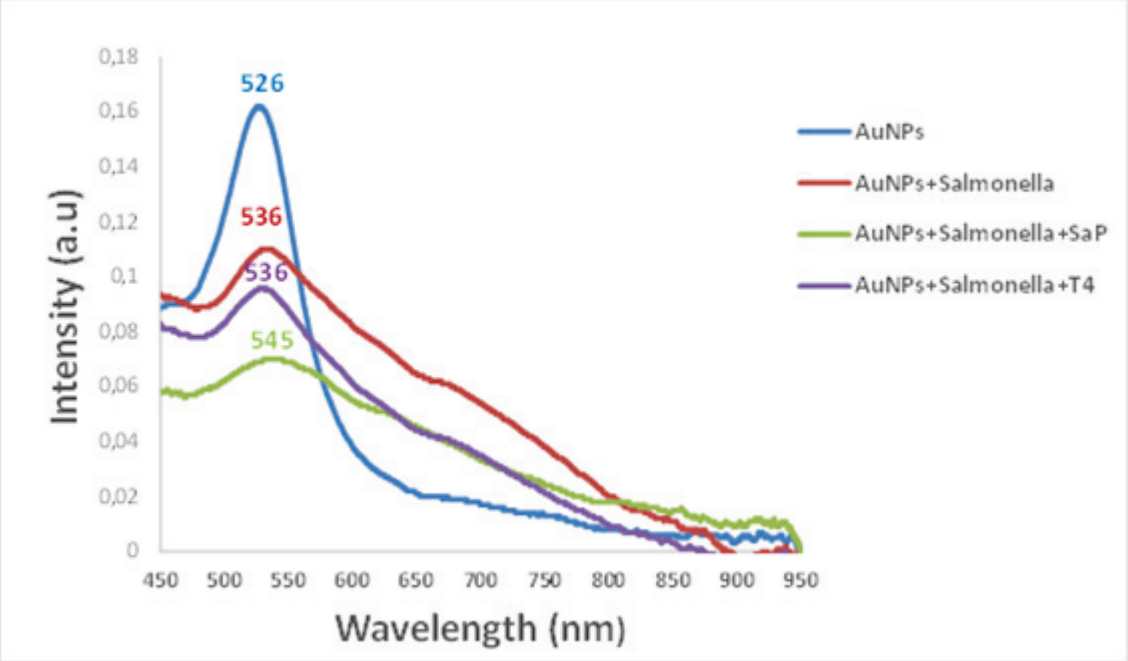

Figure 4.21. LSPR analysis of *Salmonella infantis* modified AuNPs and SaP bacteriophage interaction. AuNPs (Blue), AuNPs modified with *Salmonella infantis* (Red), Bacteriophage (SaP) Interaction with *Salmonella infantis* modified AuNPs (Green), *E.coli* phage (T4) Interaction with *Salmonella infantis* modified AuNPs (purple)

The LSPR λ_{max} of the AuNPs was measured to be 526 nm. Gold nanoparticles were incubated with *Salmonella infantis* and after washing step of excess *bacteria* on the surface, the LSPR λ_{max} was measured to be 536 nm. The LSPR λ_{max} change was almost 10 nm red-shift that was attributed to the binding of bacteria. AuNPs coated bacteria surface were then interacted with specific phage of *Salmonella infantis* (SaP) for 30 minutes and after that washing step was applied to remove unbounded phage. LSPR λ_{max} was measured to be 545 nm corresponding to a 9 nm red-shift compared with bacteria caotaed AuNPs. To display specificity of bacteria and phage interaction, bacteria coated surface was exposed to the phage of *E.coli*. In this case, the LSPR λ_{max} was measured to be 536 nm. The results show that *Salmonella infantis* was detected with its own specific phage.

Finally, AuNPs were used to detect the interaction between the specific phage of *Staphylococcus aureus* (SP) and *Staphylococcus aureus bacteria*. Figure 4.22 displays the AuNPs based LSPR spectra of bacteria - phage interactions for *Staphylococcus aureus.* In the control experiment to verify the specifity, T4 phage was used.

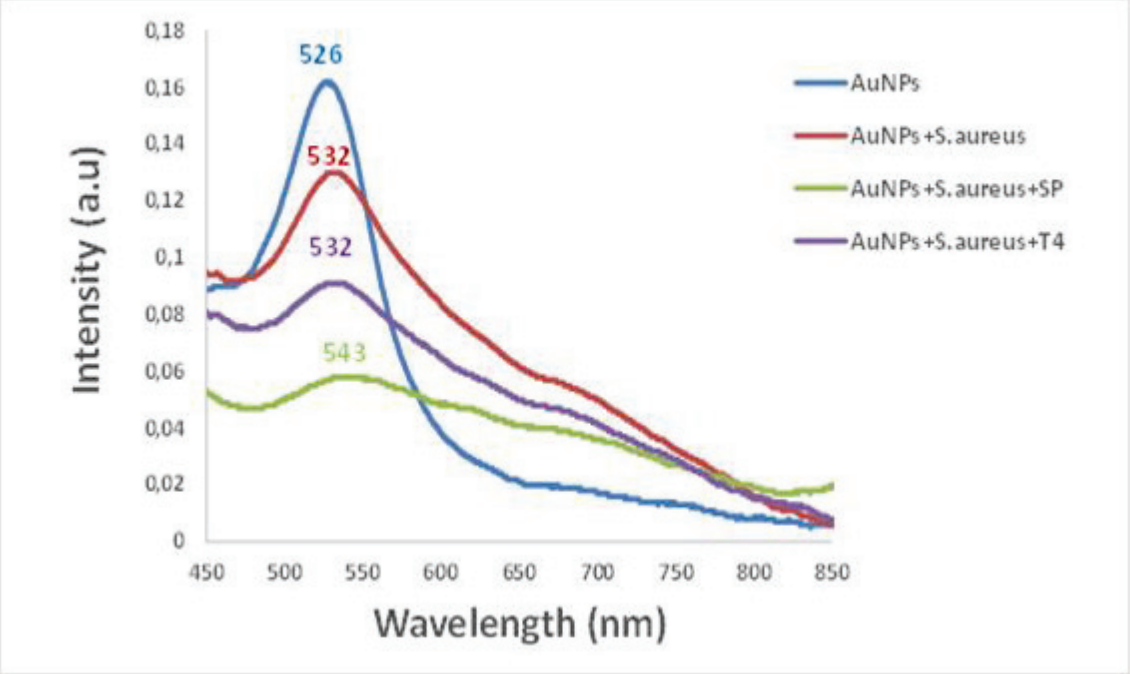

Figure 4.22. LSPR analysis of *Staphylococcus aureus* modified AuNPs and SP bacteriophage interaction. AuNPs (Blue), AuNPs modified with *Staphylococcus aureus* (Red), Bacteriophage (SP) Interaction with *Staphylococcus aureus* modified AuNPs (Green), *E.coli* phage (T4) Interaction with *Staphylococcus aureus* modified AuNPs (purple)

The LSPR λ_{max} of the AuNPs was measured to be 526 nm. AuNPs were functionalized with *Staphylococcus aureus* for 1 hours. After removing of excess *Staphylococcus aureus* on AuNPs, the LSPR λ_{max} was measured to be 532 nm. The LSPR λ_{max} change was obtained an 8 nm red-shift correspond to presence of bacteria. Then, AuNPs coated bacteria surface were then modified with SP phage for 30 minutes and after that washing step was applied to remove unbounded phage. LSPR λ_{max} was measured to be 543 nm corresponding to 11 nm red-shift in contrast to back step. To be sure detection of *Staphylococcus aureus*, T4 phage was added *Staphylococcus aureus* coated surface and in LSPR spectrum no change was observed.

The spectra clearly shows that AuNPs were modified with *Staphylococcus aureus* bacteria and the specific recognition of this bacterium by its specific phage, SP can be detected via bacteria-coated AuNPs based LSPR measurement.

CHAPTER 5

CONCLUSION

In the first part of this thesis, an LSPR spectroscopy device having different characteristics from existing systems was produced. The main difference from existing systems is the addition of microchannels potentially allowing rapid analysis at low concentrations and volumes. This design potentially makes the analysis of more than one substance to be performed at the same time through microchannels. Another significant advantage of the LSPR device produced is its ease of use and portability because of its compactness and small size, allowing the measurements to be performed in non-laboratory settings.

In the second part of the thesis, gold nanorods (AuNRs) and nanospheres (AuNPs) were successfully prepared by wet chemistry. The surface of gold nanorods was covered with a mixture of monofunctional mPEG-SH and heterofunctional SH-PEG-NH_2. LSPR anaylsis was performed to obtain the optimum PEG concentration and the appropriate composition of the PEG mixture. According to the results obtained from the LSPR results, the optimum concentration used to coat the surface of the gold nanorods was found to be 1 mM and the optimal molar ratio of mPEG-SH:SH-PEG-NH_2 to be 4:1. A model monoclonal antibody against 2-keto-3-deoxy-D-glycero-D-galacto-nononic acid (KDN), a sialic acid residue overexpressed in certain cancer cells, anti-KDN antibody was conjugated to PEGylated AuNRs and KDN molecules at varying concentrations were detected via LSPR spectroscopy. The most significant red shift was observed at 5 mM KDN concentration. Importantly, the LSPR analysis indicated that a small anionic molecule, citric acid did not bind the antibody coated AuNRs, revealing that the antiKDN-coated AuNRs was specific to the antibody's specific antigen, KDN.

In the second part, bacteria and bacteriophage interactions were investigated as a model system via AuNPs-based LSPR spectroscopy. AuNPs were first activated with *E.coli*, *Salmonella infantis* or *Staphylococcus aureus* bacteria. Specific phages of the bacteria were detected successfully via bacteria coated AuNPs-based LSPR. Importantly, the recognition was verified to be specific through control experiments performed using non-specific bacteriophages.

5.1.Future Works

The studies performed in this thesis can be further extended to include the following investigations:

1. New characteristics such as temperature sensor, software program that provides information about the binding kinetics of molecules can be included in the newly designed portable LSPR device.
2. An antibody other than anti-KDN antibody can be used to further confirm the specificity of the AuNRs based LSPR system developed. Antibody concentration on the surface can be varied and lower concentrations of analytes can be tested to investigate the sensitivity of the system.
3. Creating nanostructures, such as gold triangles, or attaching gold nanoparticles via chemical methods, on the sensor surface can be investigated to analyze samples at lower concentrations.

REFERENCES

1. Bhalla, N.; Jolly, P.; Formisano, N.; Estrela, P., Introduction to biosensors. *Essays in Biochemistry* **2016,** *60* (1), 1-8.

2. Yogeswaran, U.; Kumar, S. A.; Chen, S. M., *Nanostructured Materials for Electrochemical Biosensors*. Nova Science Publishers: 2009.

3. Qlark, L. C. J., MONITOR AND CONTROL OF BLOOD AND TISSUE OXYGEN TENSIONS. *ASAIO Journal* **1956,** *2* (1), 41-48.

4. Clark, L. C.; Lyons, C., ELECTRODE SYSTEMS FOR CONTINUOUS MONITORING IN CARDIOVASCULAR SURGERY. *Annals of the New York Academy of Sciences* **1962,** *102* (1), 29-45.

5. Updike, S. J.; Hicks, G. P., The Enzyme Electrode. *Nature* **1967,** *214* (5092), 986-988.

6. Guilbault, G. G.; Montalvo, J. G., Urea-specific enzyme electrode. *Journal of the American Chemical Society* **1969,** *91* (8), 2164-2165.

7. Yoo, E.-H.; Lee, S.-Y., Glucose Biosensors: An Overview of Use in Clinical Practice. *Sensors* **2010,** *10* (5), 4558.

8. Bergveld, P., Development of an Ion-Sensitive Solid-State Device for Neurophysiological Measurements. *IEEE Transactions on Biomedical Engineering* **1970,** *BME-17* (1), 70-71.

9. Vestergaard, M. d. C.; Tamiya, E., Nanobiosensors and Nanobioanalyses: A Review. In *Nanobiosensors and Nanobioanalyses*, Vestergaard, M. d. C.; Kerman, K.; Hsing, I. M.; Tamiya, E., Eds. Springer Japan: Tokyo, 2015; pp 3-20.

10. Suzuki, S.; Takahashi, F.; Satoh, I.; Sonobe, N., Ethanol and Lactic Acid Sensors Using Electrodes Coated with Dehydrogenase—Collagen Membranes. *Bull. Chem. Soc. Jpn.* **1975,** *48* (11), 3246-3249.

11. Schultz, J. S., Optical sensor of plasma constituents. Google Patents: 1982.

12. Liedberg, B.; Nylander, C.; Lunström, I., Surface plasmon resonance for gas detection and biosensing. *Sensors and Actuators* **1983,** *4*, 299-304.

13. Cass, A. E. G.; Davis, G.; Francis, G. D.; Hill, H. A. O.; Aston, W. J.; Higgins, I. J.; Plotkin, E. V.; Scott, L. D. L.; Turner, A. P. F., Ferrocene-mediated enzyme electrode for amperometric determination of glucose. *Analytical Chemistry* **1984,** *56* (4), 667-671.
14. Davis, J.; Huw Vaughan, D.; Cardosi, M. F., Elements of biosensor construction. *Enzyme and Microbial Technology* **1995,** *17* (12), 1030-1035.

15. Lee, Y. H.; Mutharasan, R., CHAPTER 6 - Biosensors A2 - Wilson, Jon S. In *Sensor Technology Handbook*, Newnes: Burlington, 2005; pp 161-180.

16. GS, S.; CV, A.; Mathew, B. B., Biosensors: A Modern Day Achievement. *Journal of Instrumentation Technology* **2014,** *2* (1), 26-39.

17. Mandke, R.; Layek, B.; Sharma, G.; Singh, J., Fabrication and Evaluation of Nanoparticle-Based Biosensors. In *Biosensor Nanomaterials*, Wiley-VCH Verlag GmbH & Co. KGaA: 2011; pp 73-93.

18. Kartha, K. K.; Babu, S. S.; Srinivasan, S.; Ajayaghosh, A., Attogram Sensing of Trinitrotoluene with a Self-Assembled Molecular Gelator. *Journal of the American Chemical Society* **2012,** *134* (10), 4834-4841.

19. Jolly, P.; Formisano, N.; Estrela, P., DNA aptamer-based detection of prostate cancer. *Chemical Papers* **2015,** *69* (1), 77-89.

20. Jolly, P.; Formisano, N.; Tkáč, J.; Kasák, P.; Frost, C. G.; Estrela, P., Label-free impedimetric aptasensor with antifouling surface chemistry: A prostate specific antigen case study. *Sensors and Actuators B: Chemical* **2015,** *209*, 306-312.

21. Sharma, T. K.; Ramanathan, R.; Rakwal, R.; Agrawal, G. K.; Bansal, V., Moving forward in plant food safety and security through NanoBioSensors: Adopt or adapt biomedical technologies? *PROTEOMICS* **2015,** *15* (10), 1680-1692.

22. Van Dorst, B.; Mehta, J.; Bekaert, K.; Rouah-Martin, E.; De Coen, W.; Dubruel, P.; Blust, R.; Robbens, J., Recent advances in recognition elements of food and environmental biosensors: A review. *Biosensors and Bioelectronics* **2010,** *26* (4), 1178-1194.

23. Marrazza, G.; Chianella, I.; Mascini, M., Disposable DNA electrochemical biosensors for environmental monitoring. *Analytica Chimica Acta* **1999,** *387* (3), 297-307.

24. Eltzov, E.; Pavluchkov, V.; Burstin, M.; Marks, R. S., Creation of a fiber optic based biosensor for air toxicity monitoring. *Sensors and Actuators B: Chemical* **2011,** *155* (2), 859-867.

25. Kumar, J.; D'Souza, S. F., An optical microbial biosensor for detection of methyl parathion using Sphingomonas sp. immobilized on microplate as a reusable biocomponent. *Biosensors and Bioelectronics* **2010,** *26* (4), 1292-1296.

26. Elad, T.; Almog, R.; Yagur-Kroll, S.; Levkov, K.; Melamed, S.; Shacham-Diamand, Y.; Belkin, S., Online Monitoring of Water Toxicity by Use of Bioluminescent Reporter Bacterial Biochips. *Environmental Science & Technology* **2011,** *45* (19), 8536-8544.

27. Wang, J.; Zhang, P.; Li, C. M.; Li, Y. F.; Huang, C. Z., A highly selective and colorimetric assay of lysine by molecular-driven gold nanorods assembly. *Biosensors and Bioelectronics* **2012,** *34* (1), 197-201.

28. Xu, M.; Luo, X.; Davis, J. J., The label free picomolar detection of insulin in blood serum. *Biosensors and Bioelectronics* **2013,** *39* (1), 21-25.

29. Thévenot, D. R.; Toth, K.; Durst, R. A.; Wilson, G. S., Electrochemical biosensors: recommended definitions and classification1. *Biosensors and Bioelectronics* **2001,** *16* (1–2), 121-131.

30. Kraus, D. W.; Doeller, J. E.; Zhang, X., CHAPTER 8 - Electrochemical sensors for the determination of hydrogen sulfide production in biological samples. In *Electrochemical Sensors, Biosensors and their Biomedical Applications*, Academic Press: San Diego, 2008; pp 213-235.

31. Kueng, A.; Kranz, C.; Mizaikoff, B., Amperometric ATP biosensor based on polymer entrapped enzymes. *Biosensors and Bioelectronics* **2004,** *19* (10), 1301-1307.

32. Skoog, D. A.; Holler, F. J.; Crouch, S. R., *Principles of instrumental analysis*. Brooks/Cole : Thomson Learning: Australia, 2007.

33. Purvis, D.; Leonardova, O.; Farmakovsky, D.; Cherkasov, V., An ultrasensitive and stable potentiometric immunosensor. *Biosensors and Bioelectronics* **2003,** *18* (11), 1385-1390.

34. Skládal, P., Piezoelectric biosensors. *TrAC Trends in Analytical Chemistry* **2016,** *79*, 127-133.

35. Länge, K.; Rapp, B. E.; Rapp, M., Surface acoustic wave biosensors: a review. *Analytical and Bioanalytical Chemistry* **2008,** *391* (5), 1509-1519.

36. Fan, X.; White, I. M.; Shopova, S. I.; Zhu, H.; Suter, J. D.; Sun, Y., Sensitive optical biosensors for unlabeled targets: A review. *Analytica Chimica Acta* **2008,** *620* (1–2), 8-26.

37. Damborský, P.; Švitel, J.; Katrlík, J., Optical biosensors. *Essays In Biochemistry* **2016,** *60* (1), 91-100.

38. Narayanaswamy, R.; Wolfbeis, O. S., *Optical Sensors: Industrial Environmental and Diagnostic Applications*. Springer Berlin Heidelberg: 2013.

39. Chin, C. W. S., *Localized Surface Plasmon Resonance with the Use of Silver and Titanium Oxide Nanostructures*. 2011.

40. Hong, Y.; Huh, Y.-M.; Yoon, D. S.; Yang, J., Nanobiosensors Based on Localized Surface Plasmon Resonance for Biomarker Detection. *Journal of Nanomaterials* **2012,** *2012*, 13.

41. Mayer, K. M.; Hafner, J. H., Localized Surface Plasmon Resonance Sensors. *Chemical Reviews* **2011,** *111* (6), 3828-3857.

42. Hammond, J.; Bhalla, N.; Rafiee, S.; Estrela, P., Localized Surface Plasmon Resonance as a Biosensing Platform for Developing Countries. *Biosensors* **2014,** *4* (2), 172.

43. Yuan, J.; Duan, R.; Yang, H.; Luo, X.; Xi, M., Detection of serum human epididymis secretory protein 4 in patients with ovarian cancer using a label-free biosensor based on localized surface plasmon resonance. *International Journal of Nanomedicine* **2012,** *7*, 2921-2928.

44. Yonzon, C. R.; Jeoung, E.; Zou, S.; Schatz, G. C.; Mrksich, M.; Van Duyne, R. P., A Comparative Analysis of Localized and Propagating Surface Plasmon Resonance Sensors: The Binding of Concanavalin A to a Monosaccharide Functionalized Self-Assembled Monolayer. *Journal of the American Chemical Society* **2004,** *126* (39), 12669-12676.

45. Haes, A. J.; Van Duyne, R. P., A unified view of propagating and localized surface plasmon resonance biosensors. *Analytical and Bioanalytical Chemistry* **2004,** *379* (7), 920-930.

46. Cao, J.; Sun, T.; Grattan, K. T. V., Gold nanorod-based localized surface plasmon resonance biosensors: A review. *Sensors and Actuators B: Chemical* **2014,** *195*, 332-351.

47. Liz-Marzán, L. M., Tailoring Surface Plasmons through the Morphology and Assembly of Metal Nanoparticles. *Langmuir* **2006,** *22* (1), 32-41.

48. El-Sayed, M. A., Some Interesting Properties of Metals Confined in Time and Nanometer Space of Different Shapes. *Accounts of Chemical Research* **2001,** *34* (4), 257-264.

49. Yguerabide, J.; Yguerabide, E. E., Light-Scattering Submicroscopic Particles as Highly Fluorescent Analogs and Their Use as Tracer Labels in Clinical and Biological Applications. *Analytical Biochemistry* **1998,** *262* (2), 157-176.

50. Uwe Kreibig, M. V., *Optical Properties of Metal Clusters*. Springer-Verlag Berlin Heidelberg: 1995.

51. Hutter, E.; Fendler, J. H., Exploitation of Localized Surface Plasmon Resonance. *Advanced Materials* **2004,** *16* (19), 1685-1706.

52. Gans, R., Über die Form ultramikroskopischer Goldteilchen. *Annalen der Physik* **1912,** *342* (5), 881-900.

53. Gans, R., Über die Form ultramikroskopischer Silberteilchen. *Annalen der Physik* **1915,** *352* (10), 270-284.

54. Link, S.; El-Sayed, M. A., Simulation of the Optical Absorption Spectra of Gold Nanorods as a Function of Their Aspect Ratio and the Effect of the Medium Dielectric Constant. *The Journal of Physical Chemistry B* **2005,** *109* (20), 10531-10532.

55. Link, S.; Mohamed, M. B.; El-Sayed, M. A., Simulation of the Optical Absorption Spectra of Gold Nanorods as a Function of Their Aspect Ratio and the Effect of the Medium Dielectric Constant. *The Journal of Physical Chemistry B* **1999,** *103* (16), 3073-3077.

56. Eustis, S.; El-Sayed, M. A., Determination of the aspect ratio statistical distribution of gold nanorods in solution from a theoretical fit of the observed inhomogeneously broadened longitudinal plasmon resonance absorption spectrum. *Journal of Applied Physics* **2006,** *100* (4), 044324.

57. Jensen, T. R.; Duval, M. L.; Kelly, K. L.; Lazarides, A. A.; Schatz, G. C.; Van Duyne, R. P., Nanosphere Lithography: Effect of the External Dielectric Medium on the Surface Plasmon Resonance Spectrum of a Periodic Array of Silver Nanoparticles. *The Journal of Physical Chemistry B* **1999,** *103* (45), 9846-9853.

58. Szunerits, S.; Das, M. R.; Boukherroub, R., Short- and Long-Range Sensing on Gold Nanostructures, Deposited on Glass, Coated with Silicon Oxide Films of Different Thicknesses. *The Journal of Physical Chemistry C* **2008,** *112* (22), 8239-8243.

59. Englebienne, P., Use of colloidal gold surface plasmon resonance peak shift to infer affinity constants from the interactions between protein antigens and antibodies specific for single or multiple epitopes. *Analyst* **1998,** *123* (7), 1599-1603.

60. Haes, A. J.; Zou, S.; Schatz, G. C.; Van Duyne, R. P., Nanoscale Optical Biosensor: Short Range Distance Dependence of the Localized Surface Plasmon Resonance of Noble Metal Nanoparticles. *The Journal of Physical Chemistry B* **2004,** *108* (22), 6961-6968.

61. Whitney, A. V.; Elam, J. W.; Zou, S.; Zinovev, A. V.; Stair, P. C.; Schatz, G. C.; Van Duyne, R. P., Localized Surface Plasmon Resonance Nanosensor: A High-Resolution Distance-Dependence Study Using Atomic Layer Deposition. *The Journal of Physical Chemistry B* **2005,** *109* (43), 20522-20528.

62. Zhao, J.; Jensen, L.; Sung, J.; Zou, S.; Schatz, G. C.; Van Duyne, R. P., Interaction of Plasmon and Molecular Resonances for Rhodamine 6G Adsorbed on Silver Nanoparticles. *Journal of the American Chemical Society* **2007,** *129* (24), 7647-7656.

63. Bingham, J. M.; Hall, W. P.; Van Duyne, R. P., Exploring the Unique Characteristics of LSPR Biosensing. In *Nanoplasmonic Sensors*, Dmitriev, A., Ed. Springer New York: New York, NY, 2012; pp 29-58.

64. Connolly, S.; Cobbe, S.; Fitzmaurice, D., Effects of Ligand−Receptor Geometry and Stoichiometry on Protein-Induced Aggregation of Biotin-Modified Colloidal Gold. *The Journal of Physical Chemistry B* **2001,** *105* (11), 2222-2226.

65. Malinsky, M. D.; Kelly, K. L.; Schatz, G. C.; Van Duyne, R. P., Chain Length Dependence and Sensing Capabilities of the Localized Surface Plasmon Resonance of Silver Nanoparticles Chemically Modified with Alkanethiol Self-Assembled Monolayers. *Journal of the American Chemical Society* **2001,** *123* (7), 1471-1482.

66. Nath, N.; Chilkoti, A., A Colorimetric Gold Nanoparticle Sensor To Interrogate Biomolecular Interactions in Real Time on a Surface. *Analytical Chemistry* **2002,** *74* (3), 504-509.

67. Yoo, S. M.; Kim, D.-K.; Lee, S. Y., Aptamer-functionalized localized surface plasmon resonance sensor for the multiplexed detection of different bacterial species. *Talanta* **2015,** *132*, 112-117.

68. Riboh, J. C.; Haes, A. J.; McFarland, A. D.; Ranjit Yonzon, C.; Van Duyne, R. P., A Nanoscale Optical Biosensor: Real-Time Immunoassay in Physiological Buffer Enabled by Improved Nanoparticle Adhesion. *The Journal of Physical Chemistry B* **2003,** *107* (8), 1772-1780.

69. Haes, A. J.; Chang, L.; Klein, W. L.; Van Duyne, R. P., Detection of a Biomarker for Alzheimer's Disease from Synthetic and Clinical Samples Using a Nanoscale Optical Biosensor. *Journal of the American Chemical Society* **2005,** *127* (7), 2264-2271.

70. Nguyen, H.; Park, J.; Kang, S.; Kim, M., Surface Plasmon Resonance: A Versatile Technique for Biosensor Applications. *Sensors* **2015,** *15* (5), 10481.

71. Haes, A. J.; Van Duyne, R. P., A Nanoscale Optical Biosensor: Sensitivity and Selectivity of an Approach Based on the Localized Surface Plasmon Resonance Spectroscopy of Triangular Silver Nanoparticles. *Journal of the American Chemical Society* **2002,** *124* (35), 10596-10604.

72. Dahlin, A.; Zäch, M.; Rindzevicius, T.; Käll, M.; Sutherland, D. S.; Höök, F., Localized Surface Plasmon Resonance Sensing of Lipid-Membrane-Mediated Biorecognition Events. *Journal of the American Chemical Society* **2005,** *127* (14), 5043-5048.

73. Lin, T.-J.; Huang, K.-T.; Liu, C.-Y., Determination of organophosphorous pesticides by a novel biosensor based on localized surface plasmon resonance. *Biosensors and Bioelectronics* **2006,** *22* (4), 513-518.

74. Endo, T.; Yanagida, Y.; Hatsuzawa, T., Quantitative determination of hydrogen peroxide using polymer coated Ag nanoparticles. *Measurement* **2008,** *41* (9), 1045-1053.

75. Dubas, S. T.; Pimpan, V., Green synthesis of silver nanoparticles for ammonia sensing. *Talanta* **2008,** *76* (1), 29-33.

76. Haynes, C. L.; Van Duyne, R. P., Nanosphere Lithography: A Versatile Nanofabrication Tool for Studies of Size-Dependent Nanoparticle Optics. *The Journal of Physical Chemistry B* **2001,** *105* (24), 5599-5611.

77. Xu, X.; Ying, Y.; Li, Y., Gold Nanorods Based LSPR Biosensor for Label-Free Detection of Alpha-Fetoprotein. *Procedia Engineering* **2011,** *25*, 67-70.

78. Lee, J.-H.; Kim, B.-C.; Oh, B.-K.; Choi, J.-W., Highly sensitive localized surface plasmon resonance immunosensor for label-free detection of HIV-1. *Nanomedicine: Nanotechnology, Biology and Medicine* **2013,** *9* (7), 1018-1026.

79. Bhagawati, M.; You, C.; Piehler, J., Quantitative Real-Time Imaging of Protein–Protein Interactions by LSPR Detection with Micropatterned Gold Nanoparticles. *Analytical Chemistry* **2013,** *85* (20), 9564-9571.

80. Vaskevich, A.; Rubinstein, I., Localized Surface Plasmon Resonance (LSPR) Spectroscopy in Biosensing. In *Handbook of Biosensors and Biochips*, John Wiley & Sons, Ltd: 2008.

81. Frederix, F.; Friedt, J.-M.; Choi, K.-H.; Laureyn, W.; Campitelli, A.; Mondelaers, D.; Maes, G.; Borghs, G., Biosensing Based on Light Absorption of Nanoscaled Gold and Silver Particles. *Analytical Chemistry* **2003,** *75* (24), 6894-6900.

82. Nath, N.; Chilkoti, A., Label-Free Biosensing by Surface Plasmon Resonance of Nanoparticles on Glass: Optimization of Nanoparticle Size. *Analytical Chemistry* **2004,** *76* (18), 5370-5378.

83. Fujiwara, K.; Watarai, H.; Itoh, H.; Nakahama, E.; Ogawa, N., Measurement of antibody binding to protein immobilized on gold nanoparticles by localized surface plasmon spectroscopy. *Analytical and Bioanalytical Chemistry* **2006,** *386* (3), 639-644.

84. Morokoshi, S.; Ohhori, K.; Mizukami, K.; Kitano, H., Sensing Capabilities of Colloidal Gold Modified with a Self-Assembled Monolayer of a Glucose-Carrying Polymer Chain on a Glass Substrate. *Langmuir* **2004,** *20* (20), 8897-8902.

85. Kitano, H.; Makino, Y.; Kawasaki, H.; Sumi, Y., Self-Assembled Monolayer of a Pepstatin Fragment as a Sensing Element for Aspartyl Proteases. *Analytical Chemistry* **2005,** *77* (6), 1588-1595.

86. Kitano, H.; Anraku, Y.; Shinohara, H., Sensing Capabilities of Colloidal Gold Monolayer Modified with a Phenylboronic Acid-Carrying Polymer Brush. *Biomacromolecules* **2006,** *7* (4), 1065-1071.

87. Chau, L.-K.; Lin, Y.-F.; Cheng, S.-F.; Lin, T.-J., Fiber-optic chemical and biochemical probes based on localized surface plasmon resonance. *Sensors and Actuators B: Chemical* **2006,** *113* (1), 100-105.

88. Cheng, S.-F.; Chau, L.-K., Colloidal Gold-Modified Optical Fiber for Chemical and Biochemical Sensing. *Analytical Chemistry* **2003,** *75* (1), 16-21.

89. Mitsui, K.; Handa, Y.; Kajikawa, K., Optical fiber affinity biosensor based on localized surface plasmon resonance. *Applied Physics Letters* **2004,** *85* (18), 4231-4233.

90. Kreuzer, M. P.; Quidant, R.; Badenes, G.; Marco, M. P., Quantitative detection of doping substances by a localised surface plasmon sensor. *Biosensors and Bioelectronics* **2006,** *21* (7), 1345-1349.

91. Ager, A., *Immunology Today. Immune receptor supplement*. Elsevier Trends Journals: Cambridge, 1996.

92. Davies, D. R.; Chacko, S., Antibody structure. *Accounts of Chemical Research* **1993,** *26* (8), 421-427.

93. Schroeder, H. W.; Cavacini, L., Structure and function of immunoglobulins. *Journal of Allergy and Clinical Immunology* **2010,** *125* (2), S41-S52.

94. Garcia, K. C.; Teyton, L.; Wilson, I. A., STRUCTURAL BASIS OF T CELL RECOGNITION. *Annual Review of Immunology* **1999,** *17* (1), 369-397.

95. L M Amzel, a.; Poljak, R. J., Three-Dimensional Structure of Immunoglobulins. *Annual Review of Biochemistry* **1979,** *48* (1), 961-997.

96. Harris, L. J.; Larson, S. B.; Hasel, K. W.; Day, J.; Greenwood, A.; McPherson, A., The three-dimensional structure of an intact monoclonal antibody for canine lymphoma. *Nature* **1992,** *360* (6402), 369-372.

97. Germain, R. N., MHC-dependent antigen processing and peptide presentation: Providing ligands for T lymphocyte activation. *Cell* **1994,** *76* (2), 287-299.

98. Edelman, G. M., Antibody Structure and Molecular Immunology. *Scandinavian Journal of Immunology* **1991,** *34* (1), 4-22.

99. Han, W.; Mou, J.; Sheng, J.; Yang, J.; Shao, Z., Cryo Atomic Force Microscopy: A New Approach for Biological Imaging at High Resolution. *Biochemistry* **1995,** *34* (26), 8215-8220.

100. Wu, T. T.; Kabat, E. A., AN ANALYSIS OF THE SEQUENCES OF THE VARIABLE REGIONS OF BENCE JONES PROTEINS AND MYELOMA LIGHT CHAINS AND THEIR IMPLICATIONS FOR ANTIBODY COMPLEMENTARITY. *The Journal of Experimental Medicine* **1970,** *132* (2), 211-250.

101. Chitarra, V.; Alzari, P. M.; Bentley, G. A.; Bhat, T. N.; Eiselé, J. L.; Houdusse, A.; Lescar, J.; Souchon, H.; Poljak, R. J., Three-dimensional structure of a heteroclitic antigen-antibody cross-reaction complex. *Proceedings of the National Academy of Sciences of the United States of America* **1993,** *90* (16), 7711-7715.

102. Yamaguchi, Y.; Kim, H.; Kato, K.; Masuda, K.; Shimada, I.; Arata, Y., Proteolytic fragmentation with high specificity of mouse immunoglobulin G mapping of proteolytic cleavage sites in the hinge region. *Journal of Immunological Methods* **1995,** *181* (2), 259-267.

103. Conte, L. L.; Chothia, C.; Janin, J., The atomic structure of protein-protein recognition sites11Edited by A. R. Fersht. *Journal of Molecular Biology* **1999,** *285* (5), 2177-2198.

104. Decanniere, K.; Desmyter, A.; Lauwereys, M.; Ghahroudi, M. A.; Muyldermans, S.; Wyns, L., A single-domain antibody fragment in complex with RNase A: non-canonical loop structures and nanomolar affinity using two CDR loops. *Structure* **1999,** *7* (4), 361-370.

105. Wilson, I. A.; Stanfield, R. L., Antibody-antigen interactions: new structures and new conformational changes. *Current Opinion in Structural Biology* **1994,** *4* (6), 857-867.
106. Braden, B. C.; Poljak, R. J., Structural features of the reactions between antibodies and protein antigens. *The FASEB Journal* **1995,** *9* (1), 9-16.

107. Braden, B. C.; Goldman, E. R.; Mariuzza, R. A.; Poljak, R. J., Anatomy of an antibody molecule: structure, kinetics, thermodynamics and mutational studies of the antilysozyme antibody D1.3. *Immunological Reviews* **1998,** *163* (1), 45-57.

108. Ros, R.; Schwesinger, F.; Anselmetti, D.; Kubon, M.; Schäfer, R.; Plückthun, A.; Tiefenauer, L., Antigen binding forces of individually addressed single-chain Fv antibody molecules. *Proceedings of the National Academy of Sciences* **1998,** *95* (13), 7402-7405.

109. Charles A Janeway, J., Paul Travers, Mark Walport, and Mark J Shlomchik., *Immunobiology*. Garland Science: New York, 2001; Vol. 5.

110. Breitbart, M.; Rohwer, F., Here a virus, there a virus, everywhere the same virus? *Trends in Microbiology* **2005,** *13* (6), 278-284.

111. Brüssow, H.; Hendrix, R. W., Phage Genomics. *Cell* **2002,** *108* (1), 13-16.

112. Karl, D.; Letelier, R.; Tupas, L.; Dore, J.; Christian, J.; Hebel, D., The role of nitrogen fixation in biogeochemical cycling in the subtropical North Pacific Ocean. *Nature* **1997,** *388* (6642), 533-538.

113. Rothman, D. H.; Fournier, G. P.; French, K. L.; Alm, E. J.; Boyle, E. A.; Cao, C.; Summons, R. E., Methanogenic burst in the end-Permian carbon cycle. *Proceedings of the National Academy of Sciences* **2014,** *111* (15), 5462-5467.

114. Weitz, J. S.; Poisot, T.; Meyer, J. R.; Flores, C. O.; Valverde, S.; Sullivan, M. B.; Hochberg, M. E., Phage–bacteria infection networks. *Trends in Microbiology* **2013,** *21* (2), 82-91.

115. Marshall, K. C., *Advances in Microbial Ecology*. Springer: 1983.

116. Blakely, G. W., A Genetic Switch, Third Edition, Phage Lambda Revisited. M. Ptashne. Cold Spring Harbor Laboratory Press. 2004. 154 pages. ISBN 0 87969 716 4. Price $39 (paperback). *Genetical Research* **2005,** *84* (3), 193-194.

117. Feiner, R.; Argov, T.; Rabinovich, L.; Sigal, N.; Borovok, I.; Herskovits, A. A., A new perspective on lysogeny: prophages as active regulatory switches of bacteria. *Nat Rev Micro* **2015,** *13* (10), 641-650.

118. Hyman, P.; Abedon, S. T., Bacteriophage Host Range and Bacterial Resistance. *Advances in Applied Microbiology* **2010,** *70*, 217-248.

119. Molineux, I. J.; Panja, D., Popping the cork: mechanisms of phage genome ejection. *Nat Rev Micro* **2013,** *11* (3), 194-204.

120. Romantschuk, M.; Olkkonen, V. M.; Bamford, D. H., The nucleocapsid of bacteriophage phi 6 penetrates the host cytoplasmic membrane. *The EMBO Journal* **1988,** *7* (6), 1821-1829.

121. Mattick, J. S., Type IV Pili and Twitching Motility. *Annual Review of Microbiology* **2002,** *56* (1), 289-314.

122. Samuel, A. D. T.; Pitta, T. P.; Ryu, W. S.; Danese, P. N.; Leung, E. C. W.; Berg, H. C., Flagellar determinants of bacterial sensitivity to χ-phage. *Proceedings of the National Academy of Sciences of the United States of America* **1999,** *96* (17), 9863-9866.

123. Aksyuk, A. A.; Rossmann, M. G., Bacteriophage Assembly. *Viruses* **2011,** *3* (3), 172-203.

124. Young, R., Phage lysis: Do we have the hole story yet? *Current opinion in microbiology* **2013,** *16* (6), 10.1016/j.mib.2013.08.008.

125. Wang, X.; Kim, Y.; Ma, Q.; Hong, S. H.; Pokusaeva, K.; Sturino, J. M.; Wood, T. K., Cryptic prophages help bacteria cope with adverse environments. **2010,** *1*, 147.

126. Edlin, G.; Lin, L.; Bitner, R., Reproductive fitness of P1, P2, and Mu lysogens of Escherichia coli. *Journal of Virology* **1977,** *21* (2), 560-564.

127. Ravin, V.; Ravin, N.; Casjens, S.; Ford, M. E.; Hatfull, G. F.; Hendrix, R. W., Genomic sequence and analysis of the atypical temperate bacteriophage N1511Edited by M. Gottesman. *Journal of Molecular Biology* **2000,** *299* (1), 53-73.

128. Fortier, L.-C.; Sekulovic, O., Importance of prophages to evolution and virulence of bacterial pathogens. *Virulence* **2013,** *4* (5), 354-365.

129. Siringan, P.; Connerton, P. L.; Cummings, N. J.; Connerton, I. F., Alternative bacteriophage life cycles: the carrier state of Campylobacter jejuni. *Open Biology* **2014,** *4* (3), 130200.

130. Ripp, S.; Miller, R. V., The role of pseudolysogeny in bacteriophage-host interactions in a natural freshwater environment. *Microbiology* **1997,** *143* (6), 2065-2070.

131. Łoś, M.; Węgrzyn, G., Pseudolysogeny. *Adv Virus Res* **2012,** *82*, 339-349.

132. Díaz-Muñoz, S. L.; Koskella, B., Bacteria–Phage Interactions in Natural Environments. *Advances in Applied Microbiology* **2014,** *89*, 135-183.

133. Green, H. N.; Martyshkin, D. V.; Rodenburg, C. M.; Rosenthal, E. L.; Mirov, S. B., Gold Nanorod Bioconjugates for Active Tumor Targeting and Photothermal Therapy. *Journal of Nanotechnology* **2011,** *2011*, 7.

134. Liopo, A.; Conjusteau, A.; Tsyboulski, D.; Ermolinsky, B.; Kazansky, A.; Oraevsky, A., Biocompatible Gold Nanorod Conjugates for Preclinical Biomedical Research. *Journal of nanomedicine & nanotechnology* **2012,** *Suppl 2*, 001.

135. Cho, S. K.; Emoto, K.; Su, L. J.; Yang, X.; Flaig, T. W.; Park, W., Functionalized Gold Nanorods for Thermal Ablation Treatment of Bladder Cancer. *Journal of Biomedical Nanotechnology* **2014,** *10* (7), 1267-1276.